Tornado Maintenance Investigated with High-Resolution Dual-Doppler and EnKF Analysis

JAMES MARQUIS, YVETTE RICHARDSON, AND PAUL MARKOWSKI

Department of Meteorology, The Pennsylvania State University, University Park, Pennsylvania

DAVID DOWELL

National Center for Atmospheric Research, Boulder, Colorado

JOSHUA WURMAN

Center for Severe Weather Research, Boulder, Colorado

(Manuscript received 24 January 2011, in final form 27 June 2011)

ABSTRACT

Dual-Doppler wind synthesis and ensemble Kalman filter analyses produced by assimilating Doppler-on-Wheels velocity data collected in four tornadic supercells are examined in order to further understand the maintenance of tornadoes. Although tornado-scale features are not resolved in these analyses, larger-scale processes involved with tornado maintenance are well represented.

The longest-lived tornado is maintained underneath the midlevel updraft within a zone of low-level horizontal convergence along a rear-flank gust front for a considerable time, and dissipates when horizontally displaced from the midlevel updraft. The shortest-lived tornado resides in a similar zone of low-level convergence briefly, but dissipates underneath the location of the midlevel updraft when the updraft becomes tilted and low-level convergence is displaced several kilometers from the tornado. This suggests that a location beneath the midlevel updraft is not always a sufficient condition for tornado maintenance, particularly in the presence of strongly surging outflow. Tornadoes in two other storms persist within a band of low-level convergence in the outflow air (a possible secondary rear-flank gust front), suggesting that tornado maintenance can occur away from the main boundary separating the outflow air and the ambient environment.

In at least one case, tilting of horizontal vorticity occurs near the tornado along the secondary gust front, as evidenced by three-dimensional vortex line arching. This observation suggests that a relatively cold secondary rear-flank downdraft may assist with tornado maintenance through the baroclinic generation and tilting of horizontal vorticity, despite the fact that parcels composing them would be more negatively buoyant than the preceding outflow air.

1. Introduction

Despite the obvious societal importance of tornadoes, outstanding questions remain regarding the dynamics governing several aspects of tornado behavior, particularly their maintenance. Some of the obstacles to answering these questions are the dangers and logistical complexity involved with data collection in tornadic storms and the vast computer resources required to simulate both the parent storm and the smaller-scale tornado simultaneously. Our current understanding derives from several studies that provide clues to the conditions and processes supporting tornadoes through numerical simulations (e.g., Klemp and Rotunno 1983; Wicker and Wilhelmson 1995; Grasso and Cotton 1995; Trapp and Fiedler 1995; Trapp and Davies-Jones 1997), radar and in situ observations (e.g., Brandes 1978, 1984; Dowell and Bluestein 1997; Wakimoto and Liu 1998; Markowski et al. 2002; Grzych et al. 2007; Wurman et al. 2007a,b; Hirth et al. 2008), or theory (e.g., Davies-Jones and Brooks 1993). A review of tornado-related literature suggests a strong focus on understanding tornadogenesis. Informally tallied, at least a dozen different albeit not always unrelated, hypotheses have been posed

Corresponding author address: James N. Marquis, The Pennsylvania State University, 503 Walker Building, University Park, PA 16802.
E-mail: jmarquis@met.psu.edu

DOI: 10.1175/MWR-D-11-00025.1

for methods of tornadogenesis (Davies-Jones 2006). In comparison, a relative paucity of studies exist that focus on the maintenance of a mature tornado. In fact, the authors are aware of only one study that predicts certain conditions for tornado maintenance (Dowell and Bluestein 2002, hereafter DB02). Some studies have briefly described observations of the evolution of certain storm-scale or mesocyclone-scale features that are concurrent with a weakening tornado, which may be useful for understanding how tornado maintenance is disrupted. The following is a short review of such observations and a list of some outstanding questions regarding the role that certain storm- and mesocyclone-scale processes play in tornado maintenance. Schematic diagrams of these processes are shown in Fig. 1.

1) Rear-flank downdrafts and gust fronts:

   Past works (e.g., Lemon and Doswell 1979; Brandes 1978, 1984; Wicker and Wilhelmson 1995) have emphasized a divided mesocyclone structure, outflow surrounding circulation centers, trajectories coming from outflow air, and occluded gust front structure, at tornadogenesis. However, such studies have also mentioned that similar storm-scale outflow structures are observed at tornado demise (Fig. 1a). Therefore, it is not clear to what extent changes in the outflow structure and the separation of the tornado vortex from environmental air affects tornado duration. Marquis et al. (2008) show that the tornado in the Crowell, Texas, supercell persisted while separated from the convergence on the primary rear-flank gust front by several kilometers, but located near a secondary rear-flank gust front. Signals of similar secondary rear-flank downdraft pulses have been detected in other storms with high-resolution radar data (Wurman et al. 2007a, 2010), mobile mesonet observations (e.g., Finley and Lee 2008; Lee et al. 2008; Finley et al. 2010), and numerical models (Adlerman 2003). The role that secondary surges of rear-flank downdraft and their attendant gust fronts play in tornado maintenance is not well understood.

2) Mesocyclone strength:

   DB02 summarize that ''tornado maintenance requires a continued collocation of vertical vorticity and horizontal convergence.'' Therefore, tornado maintenance is disrupted if the surrounding larger-scale circulation (e.g., mesocyclone) and/or horizontal convergence weakens, decreasing the inward transport of angular momentum (Fig. 1b), or if dissipation of angular momentum increases. Rasmussen and Straka (2007) show that the Dimmitt, Texas, tornado weakens when an axial downdraft and low-level divergence are present, resulting in the reduction of angular momentum near the axis of rotation at the ground. However, this calculation of the angular momentum budget near a tornado is performed in only one storm with single-Doppler data, precluding a comparison of their observations to the full storm-scale flow in other supercells.

3) Tornado position relative to midlevel updraft:

   DB02 hypothesize that tornadoes observed in the cyclic supercell near McLean, Texas, were maintained while their updraft-relative motion, which was approximately that of the average updraft-relative flow surrounding them, was near zero. Maintenance was disrupted when storm outflow decreased and/or storm-relative inflow increased, resulting in the tornado becoming removed from the ideal zone of convergence and tilting and stretching of vorticity located beneath the midlevel updraft (Fig. 1c). Numerical simulations by Wicker and Wilhelmson (1995) indicate a displacement of the near-surface vortex from the updraft aloft by strong outflow winds present when the tornado is weakening, consistent with visual observations of dying tornadoes (e.g., Wakimoto and Martner 1992). The generality of this result is unclear, as the effect of the mesocyclone-scale flow on the motion of the tornado and its placement relative to the main updraft in other storms is not known.

4) Outflow temperature:

   Markowski et al. (2002, 2003) found that relatively buoyant rear-flank outflow (the outflow was usually negatively buoyant, but only weakly negatively buoyant in most cases) was associated with the genesis of intense, long-lived tornadoes in the sample of storms for which surface observations were obtained (Fig. 1d). However, as tornadoes reach maturity, strong dynamically induced convergence exists in the corner flow region owing to the interaction of the tornado with the ground. On larger scales, dynamically induced vertical acceleration associated with $\partial p'/\partial z < 0$ and $\partial \zeta/\partial z > 0$ may also exist. Therefore, it is not clear if the evolution of outflow temperature affects tornado maintenance if dynamically induced low-level convergence could contract and lift negatively buoyant air.

5) Three-dimensional vorticity structure:

   Straka et al. (2007) propose that portions of baroclinically generated (horizontal) vortex rings within the rear-flank downdraft can be tilted as they descend and move forward in a storm-relative sense and encounter an elongated updraft (like that along a rear-flank gust front), generating cyclonic vertical vorticity at the ground in the typical tornado location (Fig. 1e). This baroclinic mechanism is suggested to be important to tornadogenesis. However, it is not known if it plays a significant role in the maintenance of a mature tornado.

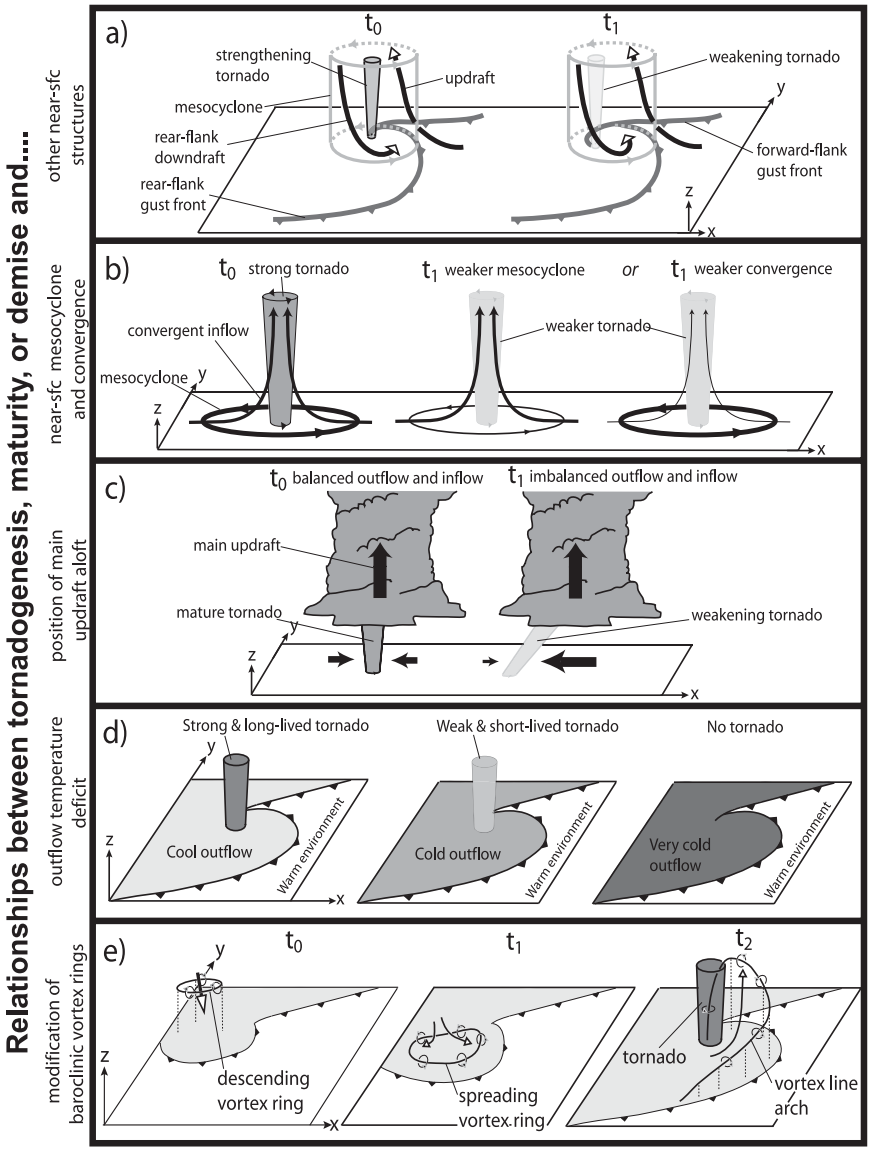

FIG. 1. Schematic representations of the five topics relating to stages of the tornado life cycle outlined in the introduction: (a) the observed relationship between the rear-flank downdraft and gust fronts, mesocyclone, and a tornado during tornadogenesis and demise; (b) the relationship between tornado strength and changes in the strength of the low-level mesocyclone and convergence; (c) the relationship between tornado strength and its position relative to the primary updraft (the horizontal arrows represent the relative magnitudes of the low-level updraft-relative inflow and outflow); (d) the relationship between tornado longevity and temperature deficit of the outflow; and (e) the relationship between tornadogenesis and the tilting of an initially sinking baroclinically generated vortex ring (thin dashed vertical lines indicate the height of the vortex line above the ground). In (a)–(e), tornadoes that are shaded with dark gray have a greater intensity than those with a lighter gray shading. Nondimensional times of images are labeled in (a),(b),(c), and (e) with $t_0 < t_1 < t_2$.

Additionally, it is not known if a similar mechanism occurs along secondary rear-flank gust fronts, sometimes collocated with a horizontal temperature gradient (e.g., Finley and Lee 2008; Finley et al. 2010) that may contribute to a complex pattern of baroclinic horizontal vorticity generation and tilting in the rear-flank downdraft.

In the present study, high-resolution ($\Delta x \sim 100$ m, $\Delta t < 60$–90 s) single- and dual-Doppler data collected by

two Doppler-on-Wheels (DOW; Wurman et al. 1997) radars in four tornadic supercells are analyzed in order to address some of the unknowns about tornado maintenance listed above. In two of the four cases, the spatial and temporal coverage of single-Doppler data is adequate for their assimilation into a numerical cloud model using the ensemble Kalman filter technique (EnKF; e.g., Snyder and Zhang 2003; Dowell et al. 2004). The EnKF analyses provide a coarser grid resolution ($\Delta x = 500$ m) than the dual-Doppler wind syntheses, but offer greater spatial and temporal coverage of the mesocyclone-scale flow and provide estimates of variables that were not observed in the field, such as temperature and humidity. We use the dual-Doppler syntheses to examine low-level kinematic characteristics of each storm, such as the evolution of the near-surface horizontal convergence along the gust fronts and mesocyclone-scale rotation, and use the EnKF analyses to evaluate the relationships between observed surface kinematic structures and unobserved features, such as the buoyancy of the outflow air and the relative position and strength of the midlevel updraft. The examination of these data in multiple cases allows us to determine if processes governing tornado maintenance vary across a sample of storms containing tornadoes with differing peak intensities and durations. This information may be valuable to increase the ability to forecast or nowcast tornado longevity. Section 2 briefly describes the peak intensity and duration of each observed tornado, as well as the dual-Doppler wind synthesis and data assimilation procedures performed in the four storms. Section 3 describes the examination of these data in the context of tornado maintenance, and section 4 summarizes the results.

2. Method

a. Cases studied

The tornadoes examined in this study were observed by the DOW radars on the following dates and locations: 3 June 1999 near Almena, Kansas; 30 April 2000 near Crowell, Texas; 5 June 2001, near Argonia, Kansas; and 22 May 2004, near Orleans, Nebraska (hereafter, each storm will be identified by these locations). In this study, tornadic vortices are identified by 1) a difference between the peak inbound and outbound values of the resolved radar radial velocity couplet (assumed to be approximately twice the vortex-relative peak tangential velocity), $\Delta V_r > 40$ m s^{-1}; 2) a distance between the inbound and outbound radial velocity maxima, $D < 2$ km; and 3) an estimated vertical vorticity, $\zeta = 2\Delta V_r/D > 0.1$ s^{-1}; all present throughout the lowest 1 km AGL for at least 2 min (similar to Alexander and Wurman 2008). The observed peak strength and duration of each tornado is provided in Table 1 using single-Doppler DOW velocities and National Climatic Data Center (NCDC) storm reports. The entire tornado life cycle is documented with the DOWs only in the Argonia storm, in which case, a small-scale pretornado Doppler velocity couplet is observed from approximately 0026 to 0032 UTC. Based on a composite of mobile and stationary DOW observations, visual reports from the DOW crew, and NCDC reports, it is surmised that the Argonia tornado is both the weakest (measured in terms of peak ΔV_r) and shortest lived in this study, the Almena tornado is the most intense and longest lived, and the Crowell and Orleans tornadoes contain a peak intensity and duration intermediate to the Argonia and Almena tornadoes. The structure and evolution of these storms are discussed in greater detail by Marquis et al. 2008 (Crowell), Dowell et al. 2002 (Argonia), Wurman et al. 2010 (Orleans), and Richardson et al. 2001 (Almena).

TABLE 1. A summary of the times (UTC) of formation and demise, the duration (min), and the peak strength (Fujita scale rating or peak ΔV_r in m s^{-1}) of sampled tornadoes taken from (top) the NCDC storm reports and estimated from (bottom) the single-Doppler DOW data for each of the four storms. For DOW observations, the threshold for determining a tornado's existence is $\Delta V_r = 40$ m s^{-1}.

Case (NCDC)	Formation	Dissipation	Duration	F scale
Almena	0000	0047	47	F3
Crowell	2101	2101	<1	F0
	2120	2130	10	F0
	2127	2134	7	F0
Argonia	0028	0030	2	F0
	0030	0030	<1	F0
Orleans	2304	2304	<1	F0
Case (DOW)	**Formation**	**Dissipation**	**Duration**	**ΔV_r**
Almena	0005–0015	0047	30–40	125
Crowell	Before 2055	2116	≥16	70
	2110	2130	20	60
Argonia	0032	0035	3	50
Orleans	≤2255	2312	≥17	105

b. Dual-Doppler wind synthesis

To facilitate the analysis of data on a common grid for dual-Doppler analysis, the radar data are aligned to an earth-relative reference frame by overlapping the pattern of ground clutter from several 0.5° elevation angle sweeps with the positions of man-made structures (such as towers, utility poles, and houses) as determined using high-resolution aerial photographs. The accuracy of each alignment is considered to be accurate within a 0.2°–0.3° azimuth range (Marquis et al. 2008). Once the data are

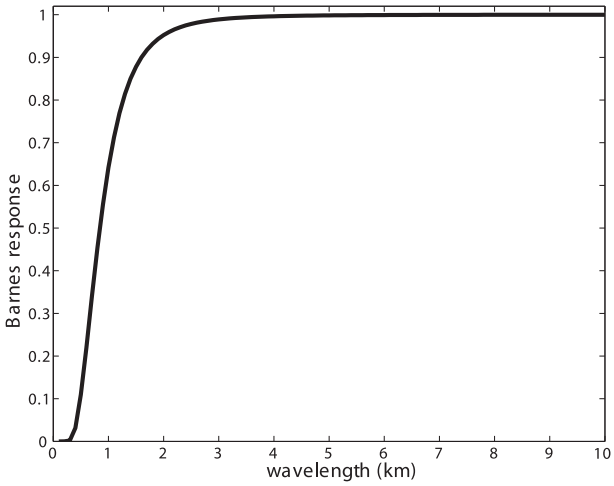

FIG. 2. The two-pass Barnes response function corresponding to objective analysis parameters used in our dual-Doppler wind syntheses.

rotated to an earth-relative framework, the ground-clutter signals are removed and aliased velocities are unfolded.

The edited DOW data are objectively analyzed to a Cartesian grid using a two-pass Barnes objective analysis technique, which minimizes the oversmoothing of well-resolved spatial scales (Majcen et al. 2008). The Barnes smoothing parameter (Barnes 1964) k is set to $(1.33\mu)^2$, as recommended by Pauley and Wu (1990), where $\mu = \phi R$ is the observed data spacing, ϕ is the beamwidth of the DOWs (0.93°), and R is the longest distance between any radar and the farthest edge of the desired portion of the dual-Doppler domain (20 km in our cases), meeting recommendations by Trapp and Doswell (2000). For all four cases, $k = 0.187$ km^2, ensuring that similar spatial scales are retained across all dual-Doppler analyses. The two-pass convergence parameter, $\gamma = 0.3$, is chosen based on the results of sensitivity tests performed by Majcen et al. (2008). The two-pass Barnes response function (Fig. 2) indicates that about 70% of the amplitude of waves with spatial scales of 1 km are retained in the analyses, while spatial scales slightly larger ($\geq$1.5 km) have a response of $>$90%.

From recommendations made by Koch et al. (1983), the Cartesian grid spacing Δ has a value between $\mu/3$ and $\mu/2$ in order to represent the resolved wavelengths while minimizing noise in spatial derivatives of the resulting wind fields. For all dual-Doppler syntheses, $\Delta =$ 150 m. Extrapolation of data to grid points outside the radar coverage is prevented by requiring that each objectively analyzed data point be influenced by observations in all surrounding octants. During the objective analysis, the horizontal positions of the data are adjusted in order to correct for motion of the velocity pattern over the time it takes to complete a full volumetric scan. The data locations are adjusted to the central time of each radar volume using a reference horizontal velocity that is estimated by tracking the motion of each tornado during the observation period. Although the motion of the tornado can deviate from the that of neighboring storm features, errors in the tilt are assumed to be fairly small; based on the usual radar scanning strategy and a typical difference in motion of the tornado and a gust front or main updraft of 5 m s^{-1} we estimate that the near-surface horizontal position of a purely vertical structure could be misaligned from its position at $z =$ 1 km by only about one horizontal grid spacing (tilt error of $\Delta x/\Delta z = 0.15$). The smoothing of features during the objective analysis reduces the influence that such a misalignment might have on our conclusions, and most of the dual-Doppler analyses performed throughout this article use data at individual levels or focus on the area very close to a tornado.

The three-dimensional wind fields are synthesized using an iterative upward integration of the anelastic mass continuity equation (with $w = 0$ m s^{-1} at $z = 0$ km) that adjusts the u, v, and w fields until the change in the resulting density-weighted w at the upper boundary of each integration layer is less than 0.01 kg m^2 s^{-1} (e.g., Dowell and Shapiro 2003). A downward extrapolation of wind data is necessary in order to apply the lower boundary condition because the lowest radar elevation angle is 0.5°, resulting in a beam height, for example, of 130 m AGL at 15 km from a radar. This extrapolation is performed in the synthesis step by setting the missing below-beam u and v wind components equal to those at the lowest level at which both radars collected data. For all dual-Doppler analyses herein, the lowest level at which both radars provide data is only one grid point above the ground; therefore, the necessary extrapolation is minimal. Corrections for the centrifuging (Dowell et al. 2005) and falling of debris and hydrometeors are not performed owing to several factors: attenuation along beams in the heavy precipitation, an uncalibrated DOW reflectivity factor, and an unknown scatterer type. The effect of hydrometeor fall speed on radial velocity is assumed to be minor because of the small antenna elevation angles used ($<$15.0°). The effect of particle centrifuging may also be minor for the resolved scales of rotation (Marquis et al. 2008).

c. EnKF data assimilation

The reader is referred to Snyder and Zhang (2003) for a comprehensive explanation of the EnKF technique as it pertains to the assimilation of radar data at convective scales. In this study, data assimilation is performed using the Data Assimilation Research Testbed software

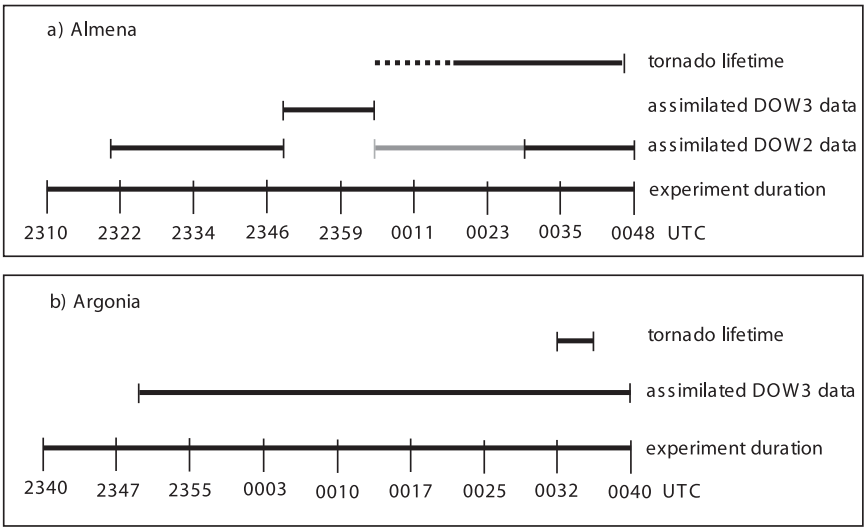

FIG. 3. Timelines of the (a) Almena and (b) Argonia EnKF experiments, including the experiment durations, the times of the assimilated DOW data, and the known lifetimes of the tornadoes. The dashed line in (a) indicates the uncertainty of the tornadogenesis time, and the gray line indicates the period of synthetic DOW2 data described in the text.

(Anderson et al. 2009). The Advanced Research Weather Research and Forecasting model (WRF-ARW; Skamarock et al. 2005) is used to perform the numerical simulation of each of the 50 ensemble members. EnKF analyses presented throughout this article represent the ensemble mean of the model fields immediately after observations are assimilated (posterior analyses).

In our experiments, an ''ensemble adjustment filter'' method is used to control the effects of an underestimated analysis-error covariance associated with using an ensemble of a finite size (Anderson 2001). Our localization factor (Hamill et al. 2001) is a compactly supported fifth-order piecewise rational correlation function from Gaspari and Cohn (1999). This function is equal to 1.0 at the location of an observation and decreases to a value of 0.0 at a distance of 6 km. Single-DOW radial velocities are assimilated at 2-min intervals. DOW sweeps are individually objectively analyzed with Cressman weighting on the original conical surfaces (Sun and Crook 2001; Dowell et al. 2004) with a horizontal grid spacing and radius of influence of 1 km. As in Dowell et al. (2004), radar velocities are assumed to have an error variance of $(2 \text{ m s}^{-1})^2$. Data from only one DOW radar are assimilated at a given time because of computational constraints, although coarse-resolution experiments in which data were assimilated from both radars (when available) yielded similar results because the additional radar either had a similar viewing angle or smaller spatial data coverage. A comparison of a dual-DOW wind synthesis and EnKF analysis using only one radar is provided in the appendix, and demonstrates that the methods produce qualitatively similar results. Based on our early feasibility experiments, which compared the EnKF solutions to dual-Doppler syntheses, at least 30 continuous minutes of DOW velocities collected throughout the lowest 3–5 km of the mesocyclone and the rear- and forward-flanks of the storm were necessary to produce coherent updraft, downdraft, and reflectivity structures. Data meeting these criteria are available only in the Almena and Argonia cases (Fig. 3). Approximately 50 continuous minutes of DOW3 data are assimilated in the Argonia case. In the Almena case, the data assimilation period is between 2320 and 0048 UTC, which includes a gap in radar data from 0004 to 0029 UTC owing to DOW redeployment. This data gap results in a presumably unrealistic evolution of the modeled storm that is not corrected until several minutes after 0029 UTC, when enough data from the second deployment have been assimilated. To prevent this unrealistic evolution, ''synthetic'' DOW observations were created at 2-min intervals between 0005 and 0029 UTC. These were based on the 0029–0030 volume of DOW3 data that was translated to appropriate locations for the earlier times during the data gap using an average storm motion. Though the resulting EnKF analyses may not be realistic during the data gap period, the modeled storm structure better resembles the observations at 0029 UTC than it does if the synthetic data are not assimilated. Our conclusions are based on analyses after 0029 UTC. Both of these storms were located at least 100 km from the nearest Weather Surveillance Radar-1988 Doppler (WSR-88D); therefore, the vertical spacing of the radar

TABLE 2. Summary of WRF implementation. Values of the Marshall–Palmer intercept parameters of graupel and rain (χ_g and χ_r), and the density of graupel (ρ_g), are the same as in Gilmore et al. (2004).

Grid sizes	$200 \times 160 \times 42$ points or $100 \times 80 \times 20$ km^3
Stretched vertical grid	150 m (near ground) $< \Delta z <$ 2 km (near top)
Time step	1 s
Open lateral boundaries	25 m s^{-1} gravity wave speed
Turbulence closure	1.5-order
Lin et al. (1983) microphysics	$\rho_g = 900$ kg m^{-3}, $\chi_g = 4 \times 10^4$ m^{-4}, $\chi_r = 8 \times 10^6$ m^{-4}
Rayleigh damping layer	Damping coef = 0.003; 15 km $< z <$ 20 km
Positive definite advection	Fifth-order horizontal; third-order vertical
Sixth-order numerical diffusion	Reduction factor = 0.12
Other parameterizations	Flat terrain Homogeneous environment No radiation No PBL parameterization

sweeps in the vicinity of each storm was approximately 1–2 km. In early feasibility experiments assimilating these data alone, updrafts initiated by warm bubble perturbations placed near the surface did not persist, indicating that the vertical density of WSR-88D data is too small to affect the EnKF results. These data are not assimilated for this reason.

Table 2 summarizes our implementation of the WRF model. A stretched z coordinate was chosen for consistency with the closer vertical spacing of the DOW data in the lowest 3 km AGL compared to that aloft. The data used to characterize the homogeneous environment varies by case. For example, the Argonia environment is based on a proximity sounding launched at Lamont, Oklahoma, located about 60 km south of the storm, about 20 min prior to the beginning of radar data collection. Unfortunately, no sounding was launched in close proximity to the inflow of the Almena storm. Instead, the base-state environment for that case is the Rapid Update Cycle (RUC) operational forecast model 0000 UTC analysis (within 15 min of the DOW intercept time of the tornado), at a model grid point within about 40 km of the DOW deployment location. The dewpoint profile was moistened between 600–350 mb so that the environment would generate a more coherent storm structure in an idealized model. Additionally, neutral or superadiabatic layers in the temperature profile for each sounding were made more stable until they had Richardson numbers slightly greater than 0.25. This modification was performed to reduce spurious convection in the simulations. Soundings for both of these cases are shown in Fig. 4. In idealized simulations, updrafts initiated by warm bubbles in these environments persisted longer than in several other environments based on modifications of the same raw soundings, but failed to persist for longer than 30–60 min. However, the storms were successfully reproduced in these environments by assimilating DOW data.

In our experiments, there are two ways by which ensemble members initially differ. First, 10 elliptically shaped warm bubbles are randomly placed within a $25 \times 25 \times 2$ km^3 box that encompasses the volume occupied by the storm at low levels near the beginning of radar observations in order to initiate the convective updrafts. Each bubble has a θ perturbation of 4 K, and a radius of 10 km in the horizontal and 1.5 km in the vertical. The placement of warm bubbles within the box is randomly different for each ensemble member. Second, random perturbations having a standard deviation of 2 m s^{-1} are added to the base-state hodographs within the lowest 11 km of the environment, thereby sustaining some ensemble spread throughout each experiment (Aksoy et al. 2009). Ensemble spread is further maintained after the initial time by Gaussian perturbations that are added to the model u, v, θ, and q_v fields every 5 min at locations where the DOW radar reflectivity factor is greater than 25 dBZ_e (Dowell and Wicker 2009). During this process, perturbations are added to T_d rather than q_v to avoid generating negative values of q_v. Dewpoint temperature is then converted back to q_v. The perturbation fields are smoothed to spatial scales of 4 km in the horizontal and 2 km in the vertical, and are added to the model fields immediately before the updated ensemble is integrated forward in time. The perturbations have a standard deviation of 1 K (for θ and T_d) and 1 m s^{-1} (for u and v) during the first 20 min of each experiment, and 0.5 K and 0.5 m s^{-1} for the remainder.

3. Results

The first goal in our study of tornado maintenance is to determine the relationship between the trends of tornado intensity and the kinematic evolution of the mesocyclone-scale circulation, the gust fronts, and the rear-flank downdrafts.

a. Mesocyclone-scale circulation

Figures 5a–d shows the relative circulation (over a circular area of expanding radius centered on the dual-Doppler vorticity maximum) given by, $\Gamma = \int_A \zeta \, dA$, and the azimuthally averaged radial velocity (in cylindrical coordinates with respect to the vertical vorticity maximum)

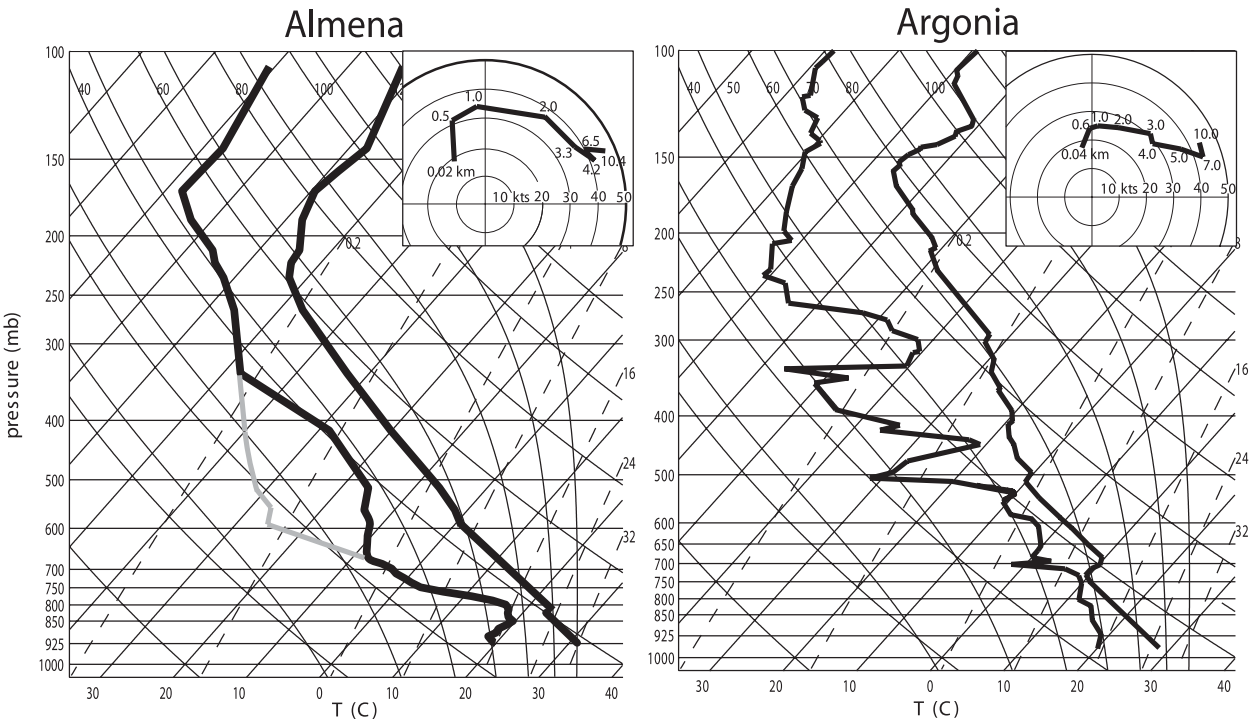

FIG. 4. Skew T–log$p$ diagrams of the homogeneous base states used in the (left) Almena and (right) Argonia EnKF data assimilation experiments. Hodographs for each case are shown in the upper right of each. Heights AGL (km) are indicated on the hodographs. (left) The unmodified RUC dewpoint profile (gray line) is shown.

as a function of time at $z = 300$ m AGL using the dual-Doppler analyses available for each storm. The trend of ΔV_r for each tornado, as observed in low-level single-Doppler radar sweeps, is shown in Figs. 5e–h. In general, the peak vortex-relative tangential wind speed ($\Delta V_r/2$) in each of the four tornadoes is maintained when mean inward radial motion is present (with spatial scales >1 km, as is retained in our objective analysis), particularly within about a 1.5-km range of the dual-Doppler vorticity maximum, such that mesocyclone-scale or tornado-cyclone-scale angular momentum is transported inward toward the axis of rotation. Tornado intensity lessens when radial inflow weakens, decreasing the inward transport of angular momentum. For example, ΔV_r in the Almena and Orleans tornadoes decreases at around 0042 and 2309 UTC, respectively, when mean inward radial velocity weakens or switches to outward velocity. The Argonia tornado develops during a period of weak inbound radial velocities at $r < 1$ km, but rapidly weakens when radial velocities become outbound. In the Crowell case, ΔV_r decreases and radial velocities are outbound at $r < 1$ km after approximately 2109 UTC, which corresponds to the period when a rear-flank downdraft surge penetrates into the vortex core, presumably causing its widening and weakening of tangential velocities (Marquis et al. 2008). It is difficult to isolate the response of tornado intensity to changes in only mesocyclone strength using these data because there are few times at which mean radial velocity is steady.

Interestingly, the two tornadoes with the highest observed wind speeds (Almena and Orleans) occur in the storms with the weakest mean mesocyclone-scale circulations at $r > 1$ km during the period of tornado maturity; whereas, the weakest and shortest-lived tornado (Argonia) occurs within the storm with the strongest circulation at these radii. Because the maintenance of the tornadoes appears to be closely tied to the ability of the mean radial flow to transport angular momentum inward toward the axis of rotation, it seems that simply the presence of a strong mesocyclone-scale circulation is not sufficient for the production or sustenance of strong tornadoes. Markowski et al. (2011) reported values of mesocyclone-scale circulation in a few nontornadic supercells similar to those in our most significantly tornadic storms. From this comparison, it appears that the kinematic property most associated with the formation and maintenance of strong and long-lived tornadoes is a persistent convergence of circulation to small radii, which was not present in their nontornadic storms. Low-level convergence and updraft in the Argonia storm may have been slightly more persistent than in the nontornadic storms, permitting the genesis of a weak and

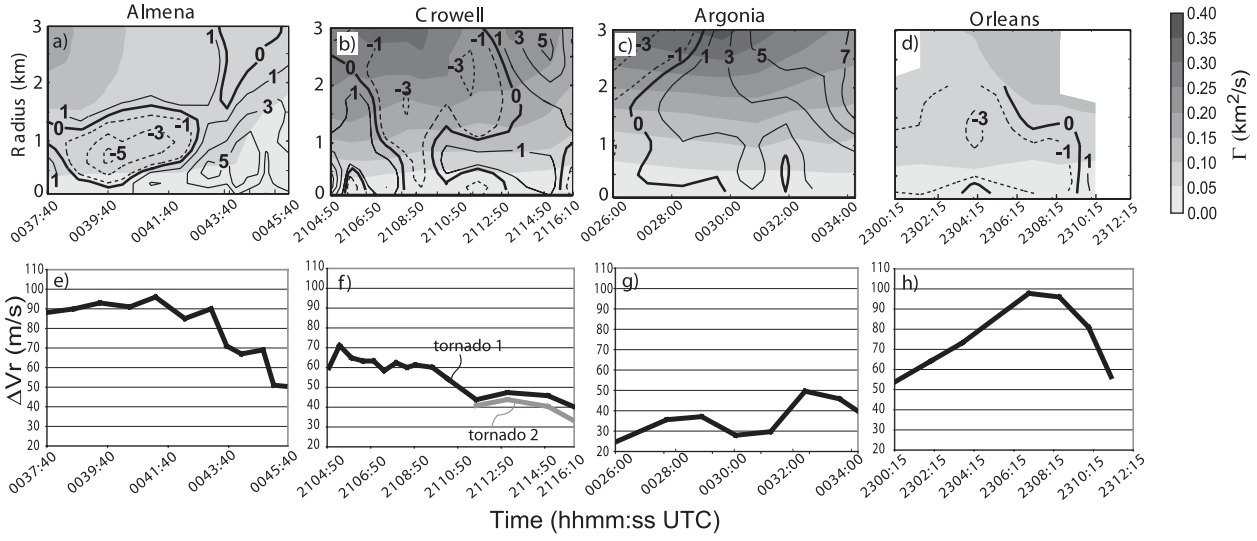

FIG. 5. (a)–(d) Circulation (shaded) and azimuthally averaged radial velocity (contours; m s^{-1}) as a function of time and radius from the axis of rotation, both measured at z = 300 m AGL in the dual-Doppler analyses for each of the four cases. Dashed (negative) contours in (a)–(d) indicate inbound radial velocities (relative to the center of rotation), solid (positive) contours indicate outbound velocities, and 0 m s^{-1} is shown with a bold contour. (e)–(h) The ΔV_r measured using unsmoothed single-Doppler data valid between z = 100–200 m AGL for each of the tornadoes.

short-lived tornado by briefly stretching the larger-scale vertical vorticity (Markowski et al. 2011).

b. Rear-flank downdrafts and gust fronts

The motion of each rear-flank gust front is examined in order to determine if the location of outflow air relative to the low-level circulation center plays a role in tornado maintenance. Figure 6 shows the ground-relative locations of the primary rear-flank gust fronts (the boundary between the environmental air and the outflow air), bands of convergence within the outflow air resembling secondary rear-flank gust fronts (observed in the Crowell, Argonia, and Orleans cases), and the tornadoes at several times in each of the four storms. The gust fronts are located by tracing the maximum in the horizontal velocity gradient tensor magnitude (Stonitsch and Markowski 2007), computed at z = 300 m in the Almena EnKF data (Fig. 6a) and the dual-Doppler data for the other three storms. (The dual-Doppler data are preferred for this analysis because of their higher resolution; however, the EnKF data are used in the Almena analysis because they provide greater horizontal coverage in that case.) The trends of the average horizontal convergence along the rear-flank gust front that coincides with the convergence immediately surrounding each tornado (measured by following the maximum of horizontal convergence along the wind shift) and the maximum value of horizontal divergence near the ground surrounding the four tornadoes are provided in Fig. 7. These calculations are performed between a 1–3-km horizontal distance from the center of each tornado, ensuring that we consider the magnitudes of horizontal convergence or divergence near the tornado that are not locally enhanced by its presence.

In the Almena storm (Fig. 6a), the intense tornado is sustained near the occlusion point of the forward- and rear-flank gust fronts, while the rear-flank gust front maintains a classic bow shape. This strong and long-lived tornado remains at least partially embedded within the convergence along the gust front for at least 25 min. After 0040 UTC, the configuration of the rear-flank gust front deforms from a spiral shape to a nearly north–south-oriented line with the weakening tornado located near its northernmost tip. After this time, no clear evidence of a forward-flank gust front exists within the observation area. During this transformation, the magnitudes of both the convergence along the gust front and the low-level divergence behind the gust front decrease (Fig. 7a; although, the convergence and divergence fields averaged in this area have greater magnitudes and decrease much more abruptly in the dual-Doppler syntheses than in the EnKF analyses, possibly owing to differences in horizontal resolution), suggesting a weakening of the rear-flank downdraft near the tornado. Thus, the tornado does not dissipate while embedded within a strengthening larger-scale rear-flank downdraft.

In the Crowell and Orleans storms (Figs. 6b,d), the primary rear-flank gust front leads each tornado by at least 4 km in the north and east directions in all dual-Doppler analyses. The Crowell tornado is far separated from the occlusion point between the forward- and rear-flank gust

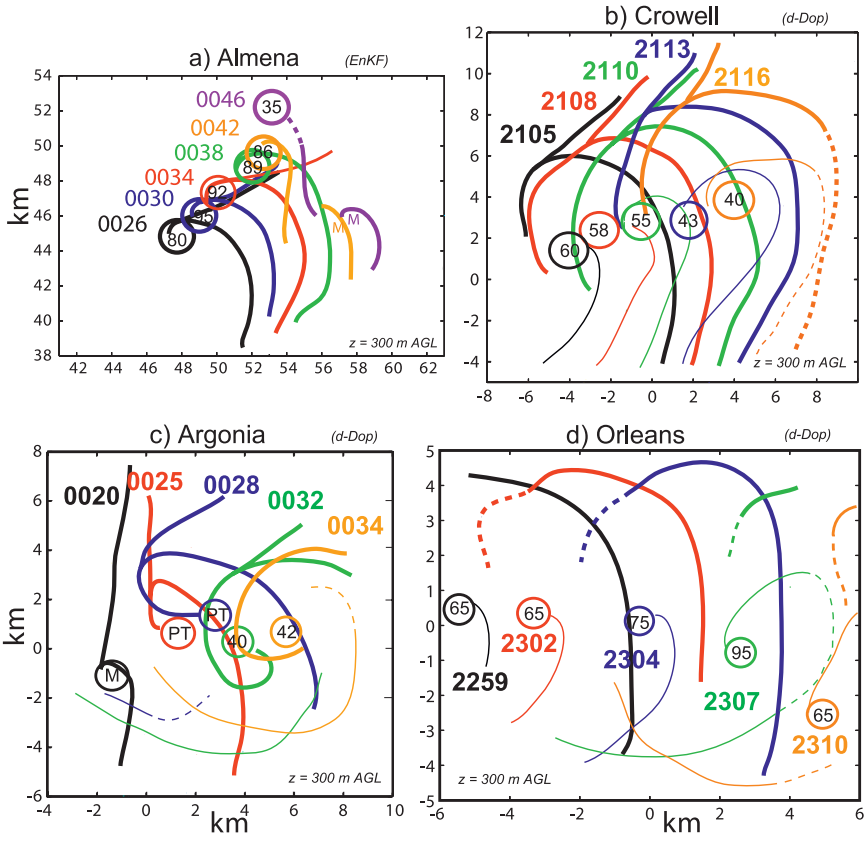

FIG. 6. (a)–(d) Ground-relative positions of the primary gust fronts (heavy lines), possible secondary gust fronts (thin lines), and tornadoes (circles) at $z = 300$ m AGL at several times in each of the four cases. The UTC time at which each tornado and gust front location is valid is indicated. The values of unsmoothed single-Doppler ΔV_r (m s^{-1}) for the tornadoes at each time are labeled within the circles. Dashed lines indicate uncertainty in the position of the gust fronts. The M in (c) denotes that the center of the mesocyclone circulation, and "PT" indicates the presence of a pretornado single-Doppler velocity couplet ($\Delta V_r < 40$ m s^{-1}). The M in (a) marks the location of a developing mesocyclone.

fronts. It is impossible to know the distance to the occlusion point in the Orleans case because a forward-flank gust front is not evident in the dual-Doppler data. Neither tornado is embedded within the convergence along the primary gust front. Instead, some of the convergence near each tornado is coincident with convergence along the secondary rear-flank gust front. A rapid forward motion of the secondary rear-flank gust front is associated with a strengthening of the convergence along it and divergence behind it in the Crowell case (Figs. 6b and 7b after 2108 UTC). Single-Doppler ΔV_r is decreasing at this time for the first tornado, owing to an increase in diameter of the vortex resulting from the apparent penetration of the secondary downdraft into its core. The second tornado forms on the periphery of the first tornado, embedded within the strong convergence along the second rear-flank gust front (Marquis et al. 2008). Wurman et al. (2010) analyze an increasing separation of the secondary gust front and the Orleans tornado in time owing to uncertainty in the connection of the strong bands of convergence located a few kilometers south of the tornado and one extending outward from near the circulation center toward the northeast in the available dual-Doppler data (thin solid lines after 2304 UTC in Fig. 6d). However, an alternative interpretation exists for this case in which the tornado remains embedded within the convergence swath along the secondary rear-flank gust front as the downdraft surge wraps around it. In the current study, we present the latter interpretation, noting the consistency of the motion of the low-level wind speed maximum associated with the outflow surge with the band of convergence spiraling outward from near the center of circulation. Thus, in the Orleans case, a rapid forward surge of the secondary rear-flank outflow starting at approximately 2304 UTC corresponds with enhanced low-level

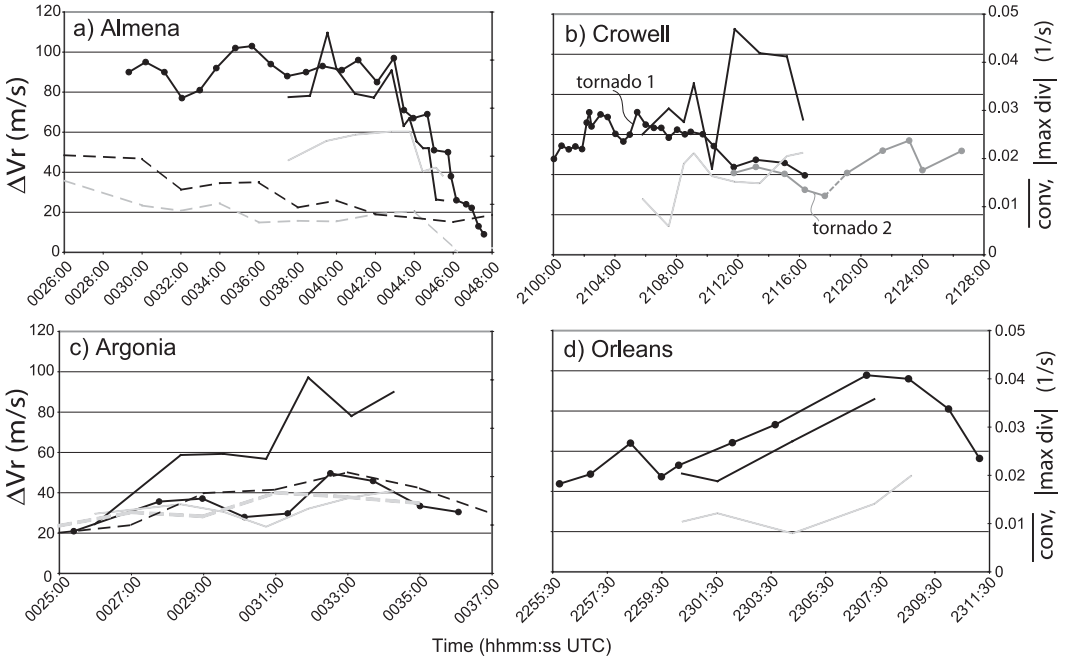

FIG. 7. (a)–(d) Trends of the unsmoothed single-Doppler ΔV_r of the tornadoes between z = 100–200 m AGL (black lines with dots), the maximum value of divergence at z = 300 m AGL between a 1–3-km range of the vertical vorticity maximum (black lines), and the average value of convergence along the gust front that contacts the resolved circulation between a 1–3-km range of the tornado (gray lines) for each of the four cases. The solid black and gray lines indicate measurements taken from the dual-Doppler syntheses in each case, and in (a),(c) the dashed black and gray lines indicate measurements taken from the EnKF analyses.

convergence along the secondary gust front near the center of circulation, and an increase in tornadic ΔV_r (Figs. 6d and 7d). In both the Crowell and Orleans cases, we speculate that each tornado dissipates while embedded within the larger-scale secondary rear-flank downdraft, causing an outward transport of mesocyclone-scale angular momentum at low levels. However, this process cannot be confirmed owing to a lack of sufficient dual-Doppler data during the last few minutes of each tornado.

In the Argonia storm (Fig. 6c), the outflow air wraps around the pretornadic and tornadic low-level circulation quite rapidly, causing the tornado to become separated from the occlusion point between the rear-flank and forward-flank gust fronts by a distance of about 10 km (distance along the gust front) in approximately 10 min. Shortly before tornadogenesis, a local strengthening of the rear-flank downdraft is found upstream of a secondary gust front located a few kilometers southwest of the circulation center (thin lines in Fig. 6c). The band of upward motion along the secondary gust front in this case initially forms south of the tornado, with subsequent northward development toward the occluded portion of the primary rear-flank gust front, remaining several kilometers away from the tornado. This evolution differs from the Crowell and Orleans cases, in which cases, the convergence along the secondary gust front is closer to the tornado. The Argonia tornado eventually dissipates while embedded within the larger-scale downdraft surge behind the secondary gust front.

In summary, tornado maintenance appears to be influenced by a continued collocation of the circulation center and mesocyclone-scale convergence, like that along a rear-flank gust front. The evolution of the rear-flank outflow in some of these storms suggests that tornadoes can be maintained by possible secondary rear-flank gust fronts while separated from the primary rear-flank gust front. Tornado dissipation may occur once collocated with a larger-scale downdraft located behind the primary, or if present, a secondary rear-flank gust front.

c. Tornado position relative to midlevel updraft

To determine if an area underneath the midlevel updraft is the ideal location of tornado maintenance in our four storms, as was hypothesized in the McLean, Texas, storm (DB02), we first determine the factors influencing the motion of our tornadoes. Figure 8 shows the ground-relative motion of the low-level dual-Doppler vertical vorticity maximum containing each of the four tornadoes. Also contoured in Fig. 8 are the relative maxima of

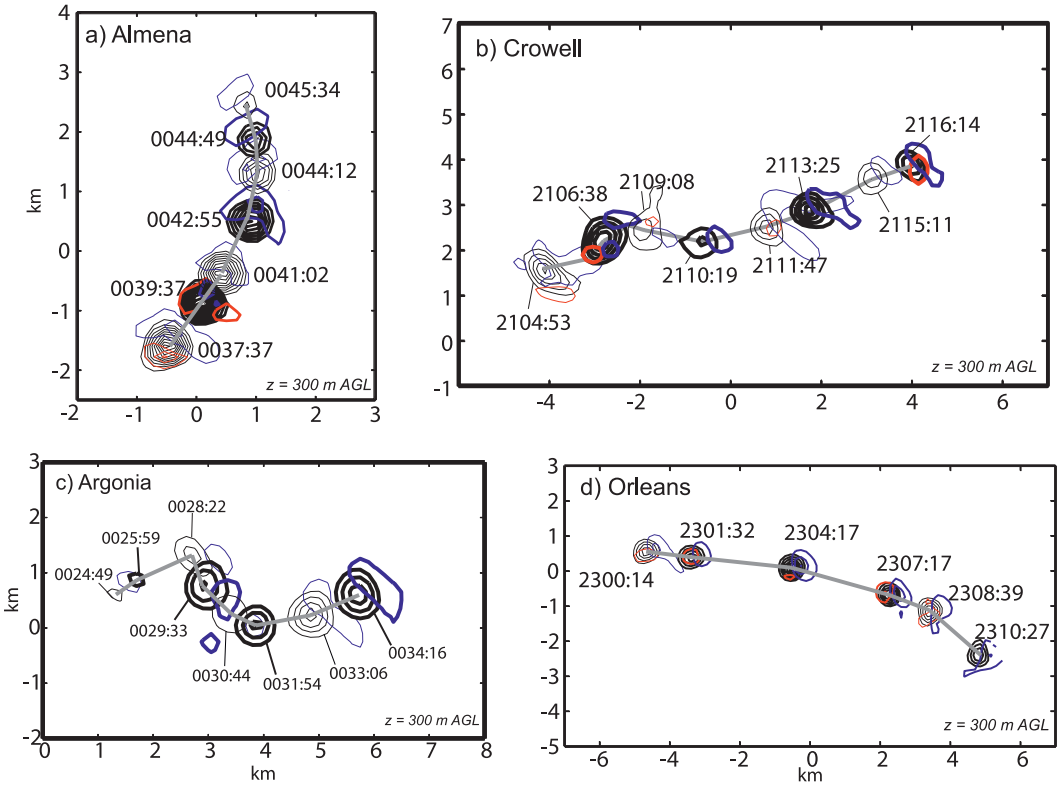

FIG. 8. Peak vertical vorticity (black contours) and the positive maxima of the advection of vertical vorticity by the ground-relative horizontal wind (blue contours) and stretching of vertical vorticity (red contours) within a 2-km horizontal distance of the tornado at several times using the dual-Doppler analyses in the (a) Almena, (b) Crowell, (c) Argonia, and (d) Orleans cases. The outermost contours of vertical vorticity are 0.08 s^{-1}, incremented by 0.003 s^{-1}. The outermost contours of terms in the vorticity tendency equation are 2×10^{-4} s^{-2}, incremented by 4×10^{-4} s^{-2}. Values of tilting and vertical advection are too small to appear in (a)–(d) based on the contour intervals chosen. The time associated with each tornado position is labeled in UTC and the height AGL of each analysis is indicated in the bottom-right corner of each. The tornado track is traced with a gray line in each.

the horizontal advection (by the ground-relative wind), vertical advection, stretching, and tilting terms in the vertical vorticity equation within a 2-km horizontal distance of the peak vertical vorticity. Near the ground, tilting and vertical advection are much weaker than the horizontal advection and stretching terms. The relative weakness of these two terms could be a partial result of the dual-Doppler estimate of the vertical motion field, which is affected by our assumed profile of horizontal convergence below the radar horizon. At almost all analysis times, the magnitude of horizontal advection is larger than that of stretching, and the resolved vertical vorticity maxima most closely follow the maxima in horizontal advection. Similar observations are made at $z \leq 1.8$ km using dual-Doppler data and at $z < 3$ km using the EnKF analyses (not shown). This implies that the tornadoes are steered by the winds in which they are embedded, consistent with DB02. Changes in the ground-relative wind field containing the low-level circulation appear to be responsible for changes in the motion of the tornadoes. For example, in the Crowell and Argonia storms (Figs. 8b,c), sudden changes in the tornado motion at 2108 and 0029 UTC (respectively) coincide with a surge in the nearby secondary outflow. However, these tornado motions deviate from the mean only temporarily, returning to their previous directions after the secondary outflow surge wraps around the center of rotation. The Orleans tornado gains a southward component of motion after approximately 2304 UTC, as it draws nearer to strong northerly winds in the secondary outflow that are originally located several kilometers to its west-northwest (see Fig. 9 in Wurman et al. 2010). In contrast to the Crowell and Argonia cases, this deviation from the original motion persists through tornado demise. The Almena tornado maintains a steady strength and northeastward motion from 0030 to 0043 UTC, but rapidly weakens after 0043 UTC, when it turns toward the northwest in the direction of the low-level environmental inflow (Fig. 8a).

The location of the midlevel updraft is estimated in the Almena and Argonia EnKF analyses. Figure 9 shows

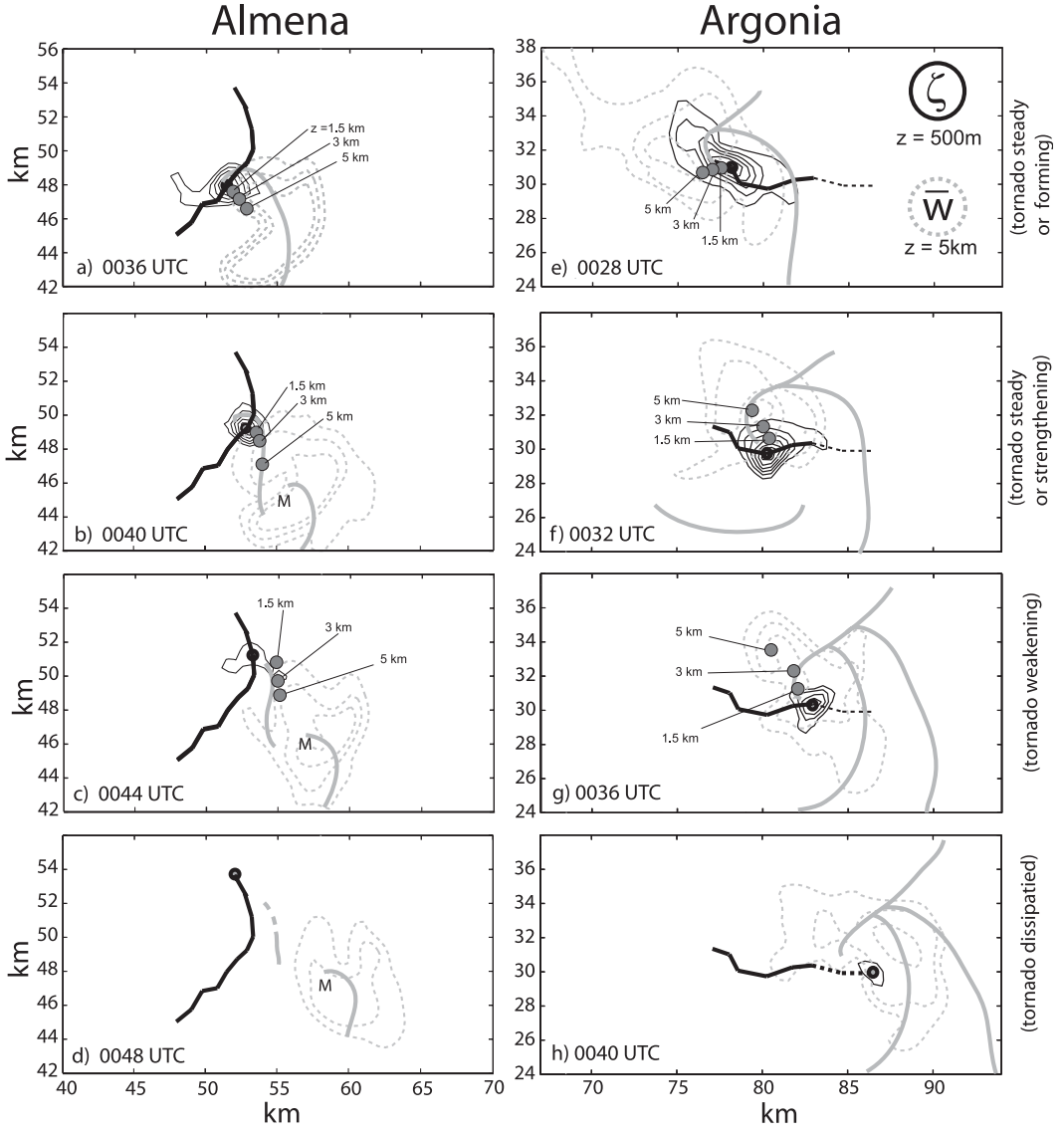

FIG. 9. (a)–(h) Ensemble-mean vertical velocity at $z = 5$ km AGL (gray dashed contours of $w = 5, 10, 15$ m s^{-1}), vertical vorticity at $z = 500$ m AGL (thin black contours; outermost contour is 0.01 s^{-1}, incremented by 0.005 s^{-1}), the position of the surface gust fronts (traced with bold gray lines), and the surface track of the tornado (thick black line) at four times in the (left) Almena and (right) Argonia EnKF analyses. The centers of the mesocyclone containing the tornado located at $z = 1.5$, 3, and 5 km AGL are shown with gray dots. A description of the tendency of the intensity of the tornadoes in each is provided on the right. The M in (b)–(d) indicates the location of a newly developing surface mesocyclone. The black dashed line in (e)–(h) indicates the path of the remnant mesocyclone after tornado dissipation.

a sequence of the ground-relative locations of the near-surface vertical vorticity maximum and the midlevel updraft in these two cases. During the observed steady-intensity portion of its life cycle, the Almena tornado is located beneath the northwestern edge of the midlevel updraft (Figs. 9a,b). A few minutes later, the rapidly weakening tornado is located at least 3 km northwest of the $w = 5$ m s^{-1} contour, indicating increasing horizontal separation from the midlevel updraft during its decay (Fig. 9c). This separation increases to about 8 km at the time that the tornado is barely discernible on radar (Fig. 9d). The tilt of the mesocyclone (illustrated with gray dots in Figs. 9a–c) increases along a northwest–southeast orientation up to tornado demise, consistent with the shear associated with a strong southeasterly inflow at low levels. Contrary to the Almena case, the Argonia tornado remains underneath some portion of the midlevel updraft throughout its entire life cycle (Figs.

9e–h). Although, the tilt of the Argonia mesocyclone also increases as it is weakening (Figs. 9e–g), consistent with vertical shear associated with the strong northwesterly outflow at low levels.

Wurman et al. (2010) speculate that the demise of the Orleans tornado also coincided with a separation from the main updraft. Though it cannot be confirmed with the dual-Doppler data, an increasing southward component of motion of the tornado associated with a collocation with the intense northerly winds in the secondary outflow surge during the last few minutes of the tornado life cycle (Fig. 8d) is consistent with this hypothesis. Therefore, the Orleans tornado may have been displaced from the midlevel updraft by surging rear-flank outflow winds, rather than by decreasing rear-flank outflow winds, as in the Almena case.

At the time of tornado demise in the Almena storm, the inflow to the midlevel updraft rises from directly beneath it, along a newly formed portion of the rear-flank gust front near which a new mesocyclone develops (Figs. 9b–d). Therefore, it appears that the area directly beneath the updraft is a favorable location for the development and maintenance of vertical vorticity at this time for this case. It is likely that the Almena tornado would not have dissipated if it had not become so displaced from the midlevel updraft after 0042 UTC. In contrast, at the time of tornado dissipation in the Argonia case, the midlevel updraft is fueled by ambient inflow that rises along the slanted surface of the primary rear-flank gust front that intersects the ground at least 5 km east of the mesocyclone (see rightmost streamline in Fig. 10i), and it persists despite diminishing low-level horizontal convergence directly beneath it. Therefore, it appears that having a tornado located beneath the midlevel updraft may not be a sufficient condition for maintenance in all storms, particularly in those with a slanted draft structure such that low-level convergence immediately surrounding the tornado may not be well correlated with updraft location aloft.

d. Outflow temperature

The EnKF analyses are used to provide estimates of unobserved thermodynamic variables to assess the relationship between changes in outflow temperature and tornado intensity in the Almena and Argonia cases. Figure 11 shows the evolution of the perturbation ensemble-mean density potential temperature (θ'_ρ; Emanuel 1994) averaged within a 2-km radius of the vertical vorticity maximum between $z = 0$ and 3 km AGL for both storms. In the Almena case, the buoyancy of the air surrounding the tornado is slowly increasing between 0026 and 0038 UTC (Fig. 11a) while the tornado is maintaining a fairly steady peak wind speed (Fig. 11b). The air composing the low-level circulation begins to cool after 0038 UTC when the tornado rapidly weakens and dissipates. Figures 10a–d show the evolution of the θ'_ρ and vertical motion fields in horizontal planes at $z = 750$ m AGL. From this sequence and from Figs. 9a–b, we see that the low-level warming shown in Fig. 11a occurs while the position of the tornado relative to the midlevel updraft and the surface gust front is constant. The cooling of the air surrounding the tornado after 0040 UTC occurs as the tornado travels toward the cold pool on the left flank of the storm. There does not appear to be a clear correlation between low-level temperature and ΔV_r during the observation period prior to 0040 UTC; the temperature increases while ΔV_r is relatively constant. It appears that the warming of the outflow air may be symptomatic of a weakening rear-flank downdraft, consistent with a decrease in the magnitude of the peak divergence and an increase in the updraft-relative wind (along with a shift in its direction toward that of the low-level inflow) near the tornado (Fig. 11b), which may have resulted in the separation of the tornado from the midlevel updraft. Trends of the convective available potential energy (CAPE), convective inhibition (CIN), and level of free convection (LFC) of parcels near the tornado at $z = 250$ m AGL, estimated by inserting the EnKF-estimated temperature and dewpoint temperature values surrounding the center of low-level circulation into the base-state sounding (Fig. 4a), are shown in Figs. 12a–c. There is a gradual decrease of CAPE (Fig. 12a) and rise in LFC (Fig. 12c) leading up to tornado demise, although these changes are relatively small (only about a 25% drop in CAPE and an 8%–10% rise in LFC). There is also an increase in CIN leading up to and beyond tornado demise, suggesting that the parcels surrounding the tornado may have had a more difficult time reaching their LFC. This may partly explain why the tornado is not maintained after approximately 0045 UTC, despite the substantial CAPE of nearby low-level parcels.

The average θ'_ρ of the air composing the low-level circulation in the Argonia storm increases throughout almost the entire life cycle of the tornado (Figs. 11c,d), because the secondary surge of outflow, which develops shortly before tornadogenesis, is warmer than the preceding pool of outflow (Figs. 10e–h). Relatively warm secondary outflows have been observed in certain mobile mesonet studies (e.g., the Dimmitt, Texas, storm in Markowski et al. 2002; Finley and Lee 2008; Finley et al. 2010), although, a diagnosis of the cause of the increasing buoyancy is not possible in those cases. Figure 10i shows a vertical cross section through this secondary downdraft (along the gray line in Fig. 10g), where a warm pocket of air protrudes downward into the cold pool south of the tornado. Increasing CAPE (Fig. 12a), decreasing CIN

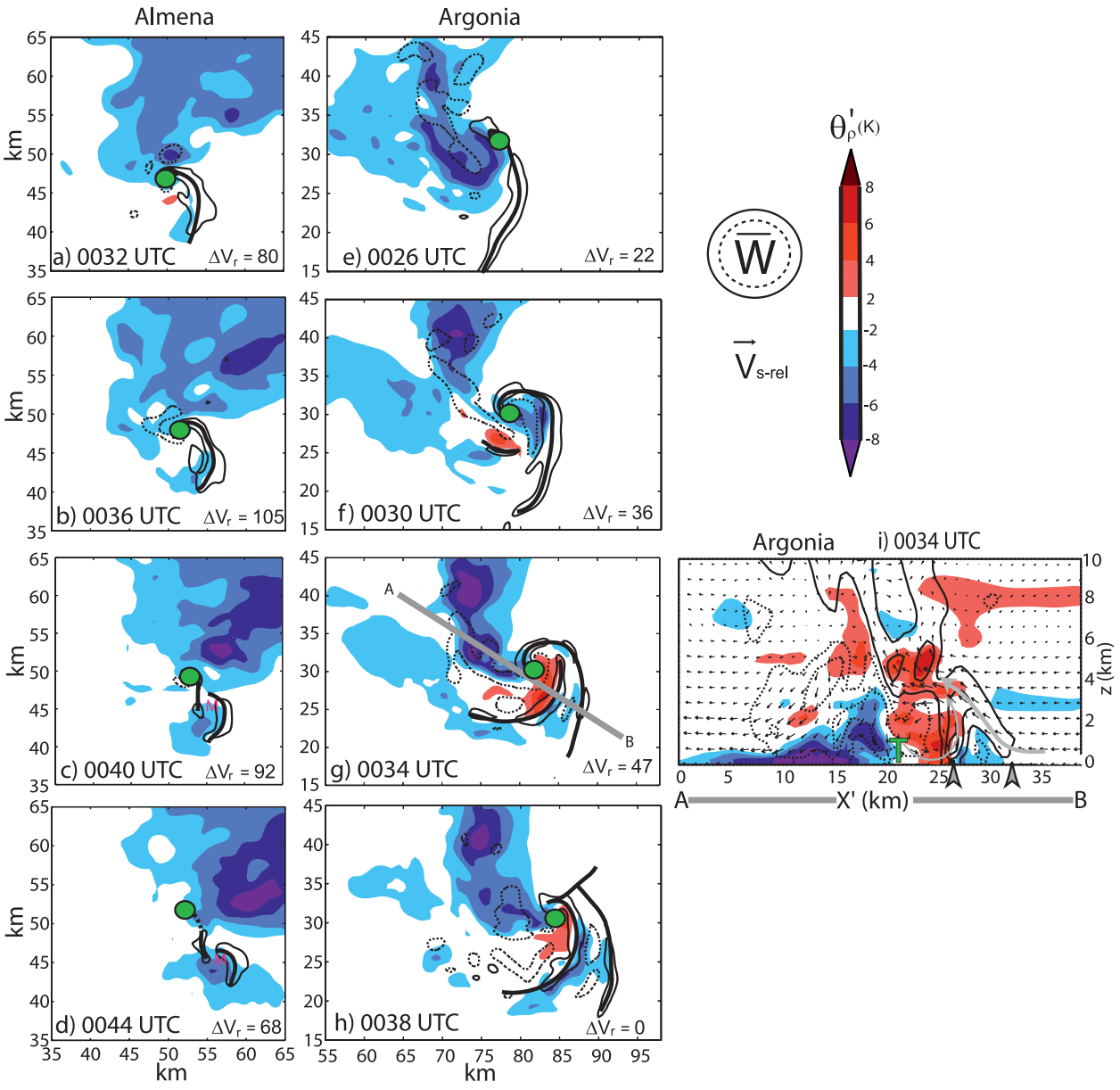

FIG. 10. (a)–(i) Ensemble-mean θ'_ρ (shaded) and vertical velocity ($w = 2$ m s^{-1} is a thin solid black contour, $w = -2$ m s^{-1} is a thin dashed black contour) at $z = 750$ m AGL in the (a)–(d) Almena storm and in the (e)–(h) Argonia storm. Surface gust fronts are traced with black lines. The location of the tornadoes are shown with green circles and the unsmoothed single-Doppler ΔV_r at each time is listed in the bottom right of (a)–(i). An M in (c),(d) indicate the location of a new mesocyclone. A vertical cross section of the same fields and storm-relative wind (vectors) along the thick gray line in (g) is shown in (i). Vertical velocity values are 2, 6, and 10 m s^{-1} (solid contours) and −2, −6, and −10 m s^{-1} (dashed contours). Gray arrows below the horizontal axis indicate where the primary gust front (right arrow) and possible secondary gust front (left arrow) intersect the ground along the cross section. The location of the tornado near the vertical cross section is indicated with a green T. Two airstreams flowing into the primary updraft are indicated with gray streamlines.

(Fig. 12b), and lowering LFC (Fig. 12c), all signals of increasing convective potential from parcels surrounding the tornado at low levels, accompany the warming of the air surrounding the tornado. Trajectory calculations of an array of parcels passing through this warm pocket of air at $z = 750$ m AGL at 0034 UTC, shown in Figs. 13a–c, demonstrate that many parcels descend within the rear-flank downdraft from altitudes of at least 3.5 km AGL (the trajectory lengths are limited by the duration of the integration period). Figure 13d shows the temperature and dewpoint temperature paths of these parcels on a skew T–log$p$ diagram (red lines) as they descend

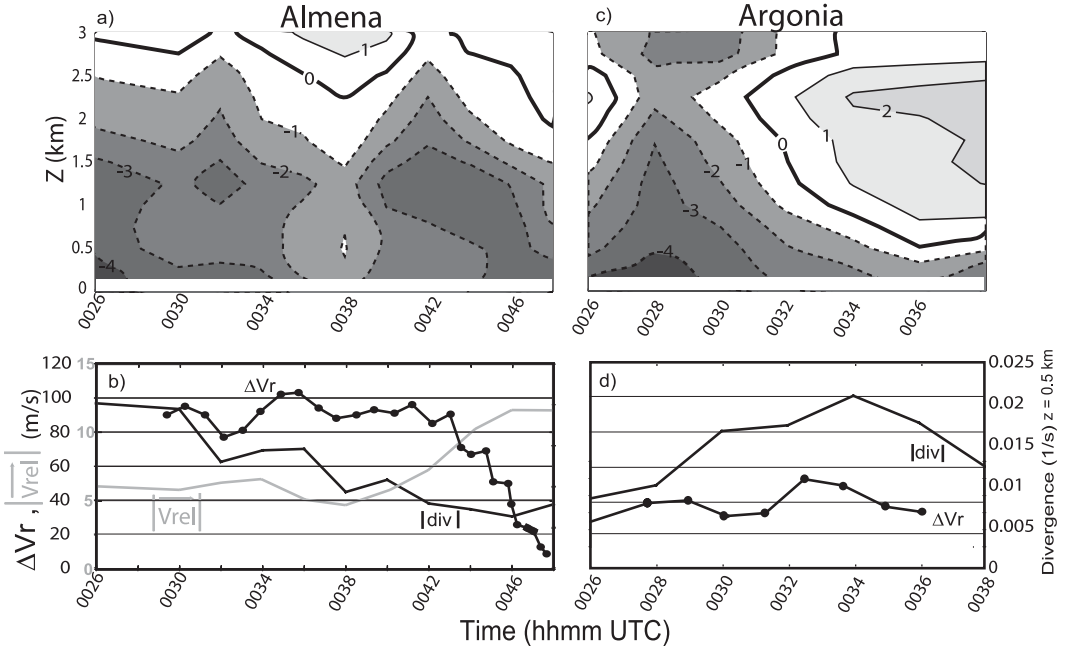

FIG. 11. (a),(c) Ensemble-mean θ'_ρ averaged within a 2-km horizontal radius of the vertical vorticity maximum as a function of time and height between $z = 0$ and 3 km AGL. The contour interval is 1 K. (b),(d) The time tendencies of the unsmoothed single-Doppler ΔV_r for the tornadoes (black lines with dots), the maximum magnitude of the horizontal divergence at $z = 500$ m AGL within a 2-km radius of the vertical vorticity maximum (black lines), and the magnitude of the horizontal updraft-relative wind averaged within a 2-km radius of the vertical vorticity maximum of the Almena storm [gray line in (b)].

within the rear-flank downdraft. An array of temperature and dewpoint profiles within the cool outflow at 0024 UTC, prior to the development of the warm secondary downdraft, also are shown in Fig. 13d (blue lines). The descending parcels are negatively buoyant a few kilometers above the ground, but become positively buoyant below 700–750 mb. This change in parcel buoyancy is reminiscent of a heat burst, resulting in relatively warm air as descending parcels overshoot their equilibrium level (e.g., Johnson 1983). However, uncertainties in the retrieval of pressure and diabatic heating terms from the EnKF analyses preclude the determination of the relative magnitudes of forcing terms in the vertical motion equation. Parcel trajectories within the warm outflow at 0034 UTC show that positively buoyant air originating in the secondary downdraft feeds a band of ascent along the secondary gust front (leftmost streamline in Fig. 10i). However, as illustrated in Figs. 6c and 10f–h, this secondary gust front is located several kilometers away from the tornado. Therefore, the parcels immediately surrounding the tornado are descending even though their CAPE (CIN) is increasing (decreasing). The resulting outward transport of mesocyclone-scale angular momentum near the ground likely prevents tornado maintenance.

In summary, the EnKF-retrieved thermodynamic fields from both cases indicate a warming of the rear-flank outflow closely preceding tornado demise, contrary to other cases documented with mobile mesonets (e.g., storm A in Markowski 2002; Finley et al. 2010). Significant values of CAPE are present in parcels surrounding each tornado, similar to the findings of Markowski et al. (2002) and Grzych et al. (2007), who found that rear-flank downdrafts generally contained more CAPE and less CIN in tornadic storms than in nontornadic storms near the time of tornadogenesis. Changes in these variables indicate a complex evolution of the outflow properties that may have affected tornado maintenance in our storms. However, it should be reiterated that in situ thermodynamic observations are not available in these cases to verify the EnKF results, which are partly influenced by microphysics parameterizations. The effect of assimilating radar data on outflow temperatures is not easily assessed in these cases because a long-lived storm is not produced in idealized simulations without data assimilation.

e. Three-dimensional vorticity structure

We examine the structure of three-dimensional vortex lines surrounding our mature tornadoes to assess the

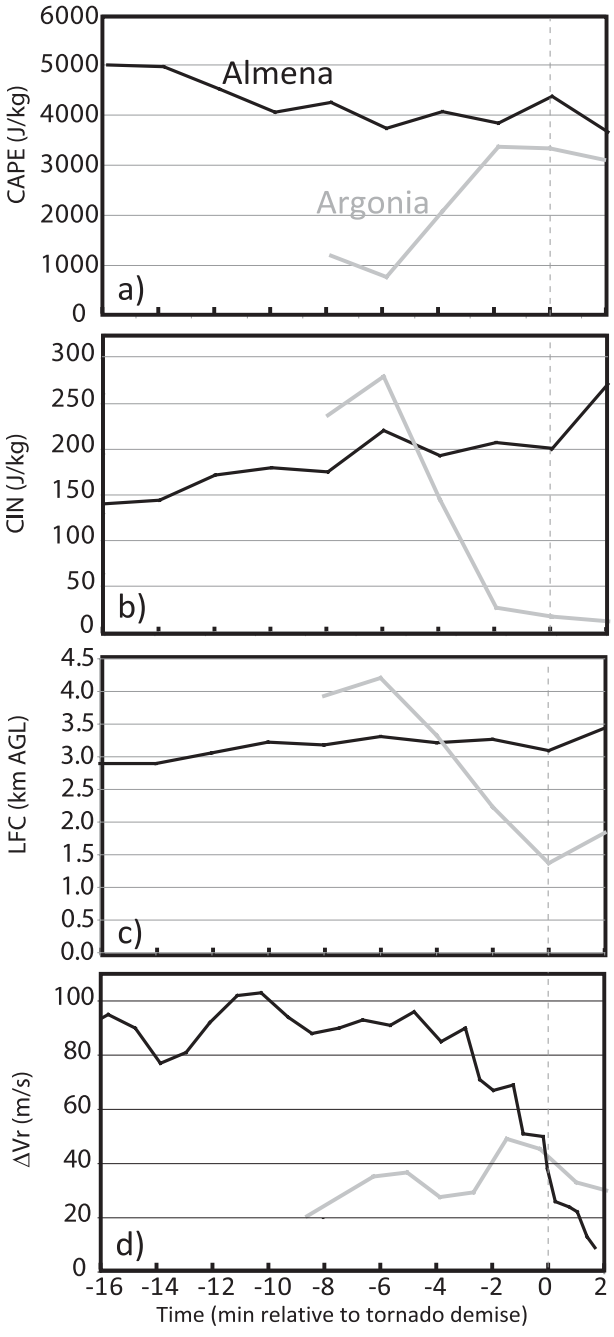

FIG. 12. The evolution of mean EnKF-estimated (a) CAPE, (b) CIN, and (c) LFC of 16 parcels encircling the Almena (black) and Argonia (gray) tornadoes at a distance of 2 km at $z = 250$ m AGL. CAPE, CIN, and LFC are estimated by inserting the temperature and mixing ratio data into the base-state sounding. (d) The trends in single-Doppler-measured ΔV_r for the tornadoes at the times corresponding to the CAPE, CIN, and LFC values. Times shown are minutes relative to the estimated time of tornado demise ($t = 0$ min).

role of the Straka et al. (2007) generation and tilting mechanism in tornado maintenance. Figure 14 shows one example from the Crowell case. Vortex lines passing through the areas of strong vertical vorticity close to the tornado are nearly upright within the dual-Doppler domain that ends at approximately $z = 2$ km AGL; therefore, these lines are not instructive regarding how the vortex connects to other features in the storm. However, when projected into a horizontal plane, several other three-dimensional vortex lines parallel the primary and the secondary rear-flank gust fronts. The vertically oriented portions of the vortex lines passing through the horizontal gradient of updraft along the occluded portion of the primary rear-flank gust front west-northwest of the tornado (e.g., orange lines passing through $x = 0$ km, $y = 1.5$ km in Fig. 14) appear to be separated from the tornado by a horizontal distance of at least 3 km. Trajectory calculations performed in this area show that parcels located at radii greater than about 3 km from the tornado orbit the low-level circulation at a constant radius or diverge outward from it (Marquis et al. 2008), suggesting that vertical vorticity produced along the primary gust front does not approach the tornado. Vortex lines near the secondary gust front pass through the area of positive vertical vorticity east-northeast of the tornado at $z = 400$ m AGL (red and blue lines in Fig. 14), many within a 2-km horizontal distance of the vorticity maximum. Trajectories calculated in this area show many parcels orbiting the low-level circulation at a nearly constant radius from its center (Marquis et al. 2008), suggesting that vertical vorticity generated along the secondary gust front remains near the tornado. The dual-Doppler analyses used in these calculations do not capture strong convergence that may exist near the ground in the vicinity of the tornado; therefore, it is possible that some of these parcel trajectories may be drawn into the tornado. These observations suggest that the secondary gust front may represent the leading edge of vortex lines generated and tilted in the descending air of the outflow surges, similar to the Straka et al. (2007) mechanism.

The orientation of the vortex lines along the secondary gust front is consistent with a secondary outflow surge that is colder than the preceding outflow. In the idealized simulations by Markowski et al. (2003), cold downdrafts inhibited the penetration of high angular momentum air to a small radius at low levels. Although the axisymmetry of the Markowski et al. simulations precludes tilting of baroclinically generated horizontal vorticity, their results might still be applicable to three-dimensional flows in the following way: horizontal vorticity that is baroclinically generated in a three-dimensional flow and subsequently reoriented into vertical vorticity

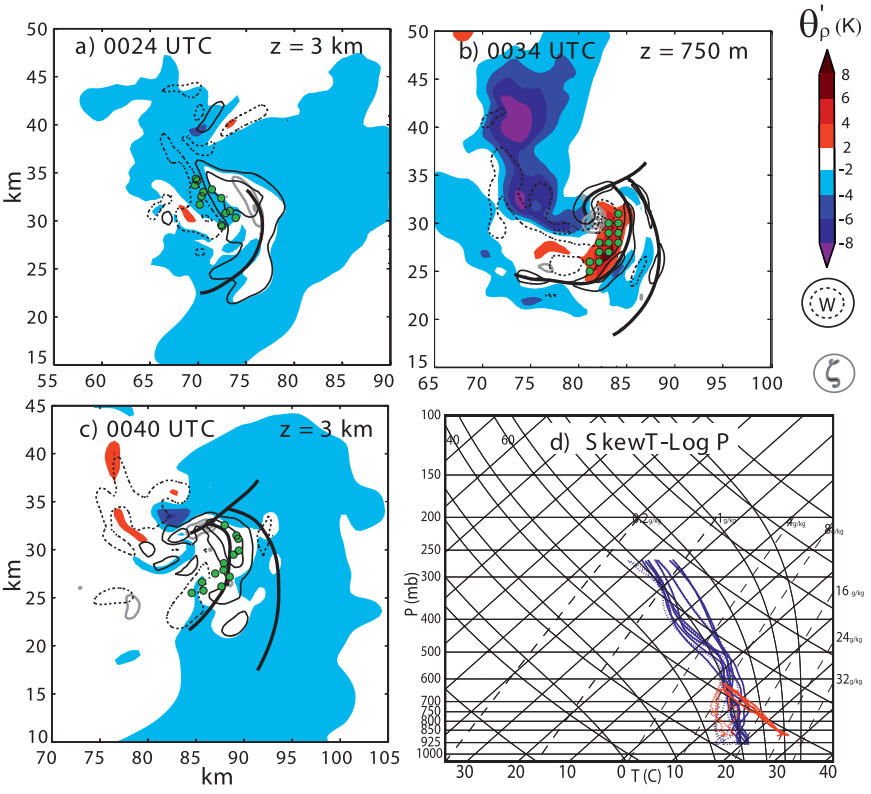

FIG. 13. (a)–(c) Ensemble-mean θ'_ρ (shaded) and vertical motion (black contours; solid contours are $w = 4$ and 12 m s^{-1} dashed contours are $w = -4$ and -12 m s^{-1}) at (a),(c) $z =$ 3 km AGL and (b) $z = 750$ m AGL, and vertical vorticity (gray contours; outermost is 0.015 s^{-1}, incremented by 0.01 s^{-1}) at $z = 750$ m AGL in the Argonia case. Surface gust fronts are traced with thick black lines in each panel. The horizontal ground-relative positions of parcels that pass through the warm secondary downdraft at $z = 750$ m AGL at (b) 0034 UTC, are shown with green dots in each. (d) Skew T–log$p$ diagrams of vertical thermodynamic profiles collected at several model grid points in the outflow air southwest of the tornadogenesis site at 0024 UTC (blue lines) before the development of the secondary downdraft and the thermodynamic profiles along the parcel paths traversing the warm secondary downdraft between 0020 and 0034 UTC (red lines).

by tilting might only be able to be intensified to tornado strength by stretching if the parcels are not too negatively buoyant.

The tilting and concentration of vertical vortex lines near a mature tornado associated with a cold secondary downdraft could imply two scenarios that are occurring in the storm: 1) parcels in the new cold outflow surge are not so negatively buoyant that they cannot be lifted, similar to those in the preceding outflow air in the pretornado stage of the storm; or 2) strong horizontal convergence in the corner flow region of the mature tornado may be sufficient to contract the colder outflow and lift parcels to their levels of free convection (if they exist). Therefore, the present case suggests that relatively cold rear-flank outflow surges (relative to previous outflow surges) may assist with tornado maintenance through the injection of favorably oriented vortex lines despite the fact that more negatively buoyant air may be entering the tornado. Though, perhaps the final outcome depends on the relative importance of the two effects. In the Crowell case, the eventual surge of the secondary downdraft around the low-level circulation center implies that the temperature of the outflow air may have further decreased such that it could not be lifted near the relatively weak tornado or it was assisted by dynamically induced downward pressure gradient forces.

4. Discussion and conclusions

A combination of high-resolution dual-Doppler wind syntheses and ensemble Kalman filter analyses produced with Doppler-on-Wheels data was examined in order

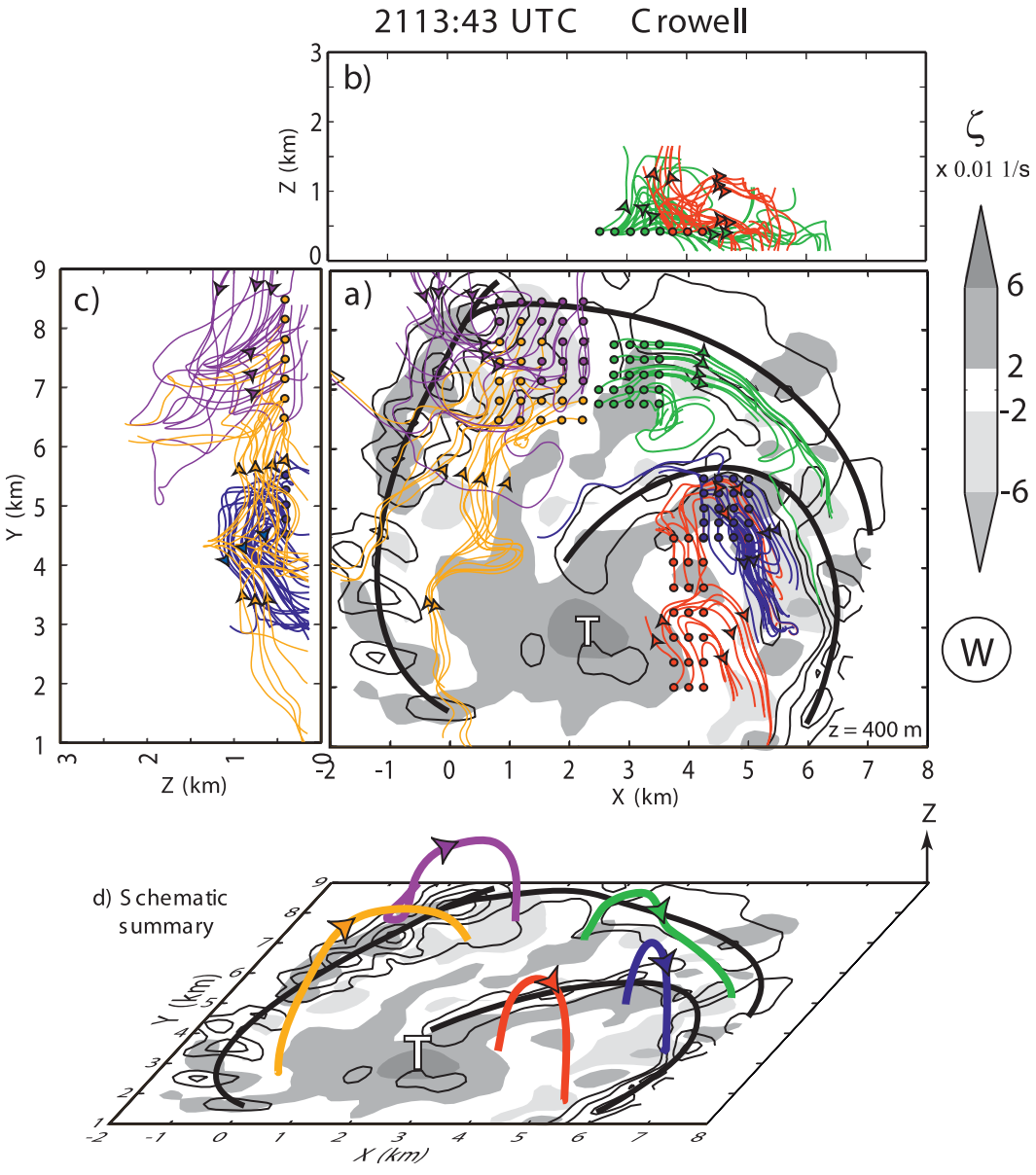

FIG. 14. (a) Dual-Doppler vertical vorticity (shaded) and vertical motion (contours; outermost contour is 1 m s^{-1}, incremented by 4 m s^{-1}) at z = 400 m AGL valid at 2113:43 UTC for the Crowell case. The gust fronts are traced using thick black lines. (b),(c) A projection of the vortex lines into the x–z and y–z planes. A T marks the location of the tornado in the horizontal plane. Purple and orange (red, green, and blue) dots indicate where vortex lines of those colors intersect areas of negative (positive) vertical vorticity at z = 400 m. The arrowheads indicate the orientation of several vortex lines. (d) A three-dimensional summary of the orientation of several vortex lines.

to determine how changes in storm structure influence the maintenance of tornadoes in four supercell storms. Figure 15 compares the evolution of the prominent storm-scale and mesocyclone-scale features on the rear-flank of the storm throughout the mature and decaying stages of the tornadoes in each of these cases to a conceptual model summarized in Lemon and Doswell (1979).

The strongest and presumably longest-lived tornado (Almena case; Fig. 15a) was at least partially embedded within the convergence along the primary rear-flank gust front (i.e., the boundary between the cool outflow and the ambient environment) for a considerable time. The tornado began to weaken shortly after the magnitude of the rear-flank downdraft decreased, rear-flank outflow temperatures increased, and the updraft-relative

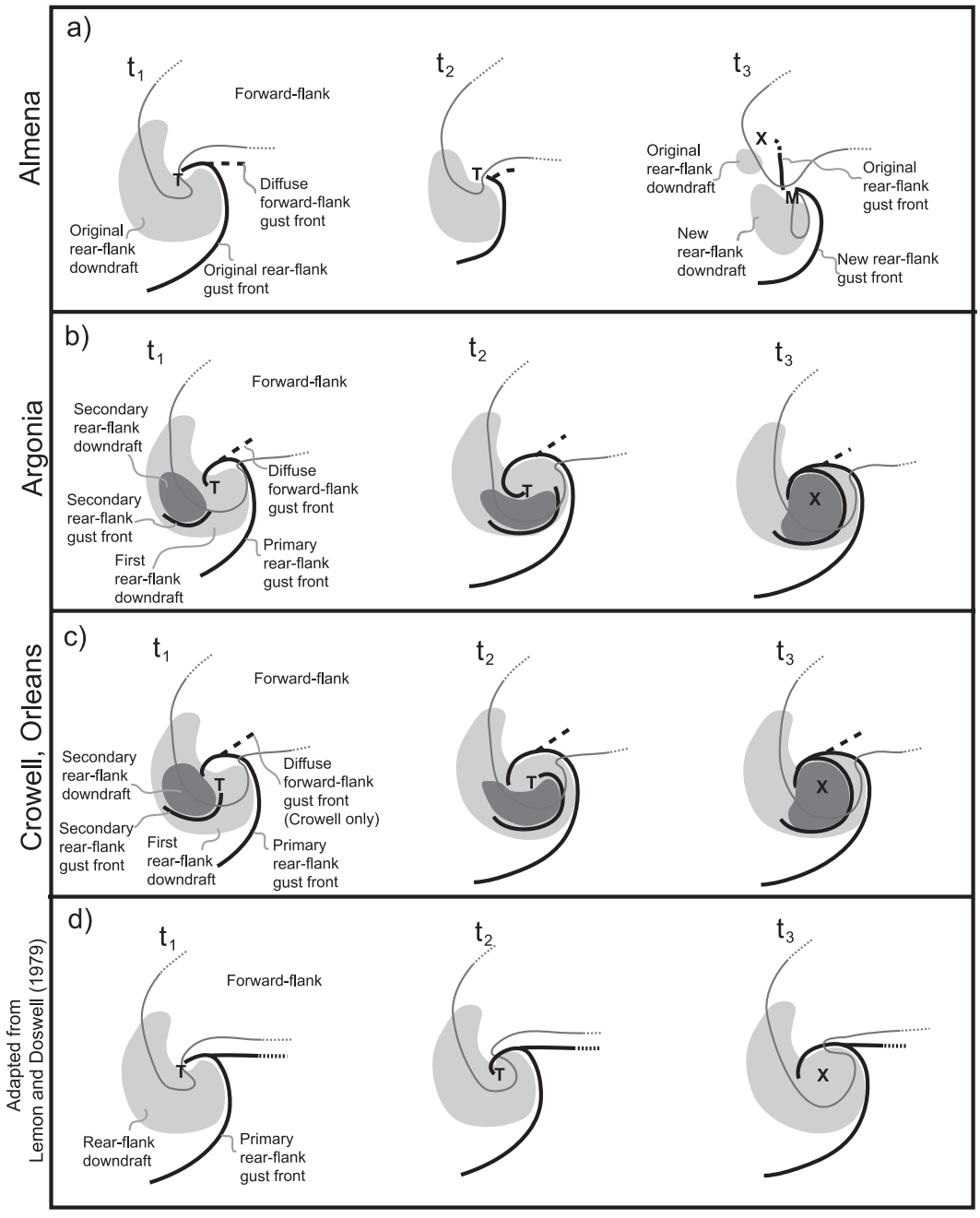

FIG. 15. A schematic illustration of the evolution of storm-scale features located on the rear-flank of the storm during tornado maturity ($t_1 - t_2$) and at the time of demise (t_3) in (a) the Almena storm, (b) the Argonia storm, and (c) the Crowell and Orleans storms. (d) A conceptual model of a supercell that does not include a secondary rear-flank downdraft and secondary gust front (adapted from Lemon and Doswell 1979). In (a)–(d), t_2 represents a time immediately before a rapid decline in tornado intensity. A T marks the location of the tornado at $t_1 - t_2$, an X marks the location of tornado demise at t_3, and an M marks the location of mesocyclogenesis in the Almena storm at t_3. Black lines indicate the presence of kinematic gust front boundaries, gray shades indicate varying magnitudes of low-level divergence associated with the rear-flank downdraft, and gray contours indicate radar reflectivity. Fine dashed lines indicate that the feature continues beyond the area shown in (a)–(d). Long dashed lines indicate uncertainty in the location of the feature.

winds surrounding the low-level circulation became prominently oriented in the direction of the low-level environmental inflow. Tornado intensity diminished when it became horizontally displaced from the midlevel updraft by several kilometers to the northwest, where nearby low-level convergence diminished and EnKF-estimated CIN was greater than for parcels surrounding the mature tornado.

The weakest and shortest-lived tornado (Argonia case; Fig. 15b) resided near the convergence along the primary rear-flank gust front for only a few minutes. Thus, the tornado dissipated when the larger-scale convergence immediately surrounding it diminished and it became collocated with a larger-scale downdraft behind a secondary rear-flank gust front, which precluded any further stretching of positive vertical vorticity near the ground. A warm secondary surge of outflow, resembling a heat burst, did not directly aid tornado maintenance because the positively buoyant outflow air did not ascend within the tornado.

A secondary rear-flank downdraft surge and gust front were observed in both the Orleans and Crowell cases (Fig. 15c). The tornadoes in these two cases were maintained while influenced by the low-level convergence present along secondary rear-flank gust fronts rather than along the primary rear-flank gust fronts, as in the Argonia and Almena cases and in many conceptual models. Vortex line arches present in the dual-Doppler data from the Crowell case suggest that the secondary rear-flank outflow was colder than the outflow air that it replaced, and that the secondary gust front tilted baroclinically generated horizontal vorticity near the tornado, possibly assisting its maintenance. A schematic diagram of this scenario is shown in Fig. 16. We speculate that the Crowell and Orleans tornadoes decayed as the low-level mesocyclone-scale convergence surrounding them was replaced with divergence from the secondary downdraft surge.

A comparison of these analyses yields the following conclusions about tornado maintenance for our four supercells:

1) Changes in the magnitude of the rear-flank downdraft preceded a disruption of tornado maintenance, but these changes varied. In three cases, we hypothesize that tornado decay occurred when each tornado became embedded within strong rear-flank downdraft. In the Almena case, however, tornado decay was preceded by a weakening of the rear-flank outflow winds.
2) Each of the tornadoes were maintained while at least partially embedded within or located near the convergence along rear-flank gust fronts, assisting the inward transport of the low-level mesocyclone circulation. Tornado maintenance is disrupted by a decrease of low-level convergence, and, therefore, a decrease of the inward transport of larger-scale angular momentum. Tornado intensity and duration appear to be governed more by the ability of a storm to transport angular momentum inward toward the axis of rotation rather than by the strength of the mesocyclone. However, if the mesocyclone is disrupted completely, tornado duration may be limited.
3) Convergence and modification of vorticity along secondary rear-flank gust fronts may help maintain tornadoes that are unconnected to primary rear-flank gust fronts. The wrapping of the secondary outflow completely around the tornado likely contributes to tornado decay, similar to the behavior of the primary rear-flank outflow in previous conceptual models of tornadic supercells.
4) A tornado being located directly underneath the midlevel updraft may not be a sufficient condition for maintenance, particularly if low-level convergence surrounding the tornado weakens while the updraft persists. In the cases in which it is believed that the tornado dissipated because of a separation from the main updraft (Almena and Orleans), one was displaced by strong inflow winds and the other by horizontal winds in a rear-flank downdraft surge.
5) The EnKF-estimated thermodynamic data in the Almena and Argonia cases suggest that warming rear-flank outflow air may not have directly aided in tornado maintenance. In both cases, the warming appeared to be a product of processes that adversely affected tornado maintenance (a weakening rear-flank downdraft in the Almena case, and a possible heat burst in the Argonia case).
6) Although the presence of cold outflow air may hinder horizontal convergence and associated stretching of

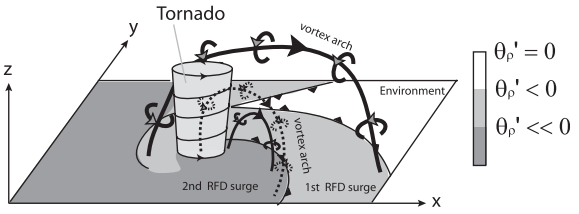

FIG. 16. Schematic illustration of vortex line arches associated with multiple rear-flank outflow surges of decreasing near-surface θ_ρ relative to the environment (shaded). Primary and secondary gust fronts are indicated with thin black lines and the vortex lines are shown with rings and arrow heads to indicate their orientation. The dashed vortex line indicates a vortex arch along the secondary gust front that is speculated to pass through the tornado, but may not have been observable in our data.

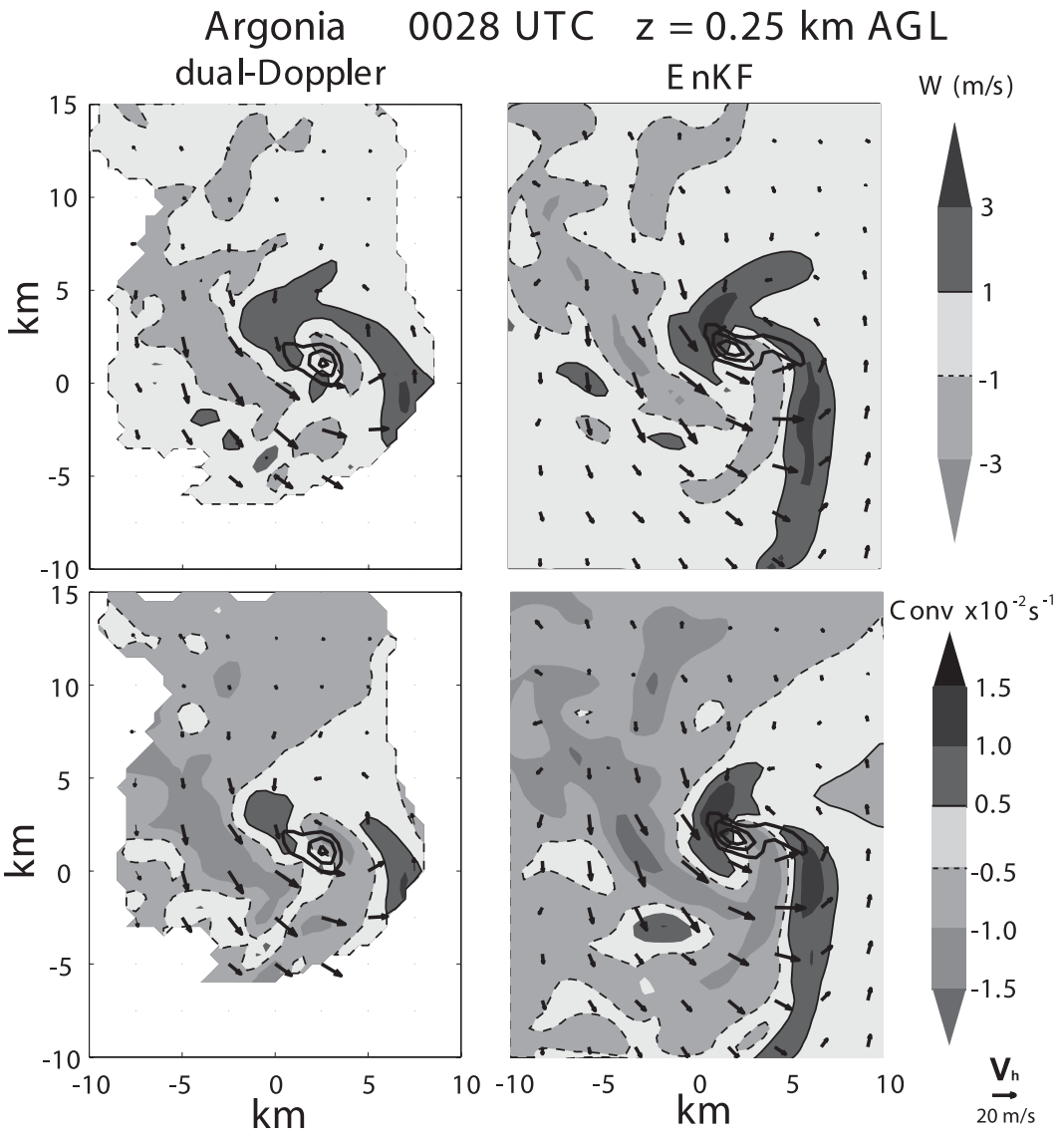

FIG. A1. (top) Vertical velocity (shaded), vertical vorticity (contoured; outermost contour is 0.02 s^{-1}, incremented by 0.01 s^{-1}), and ground-relative horizontal wind (vectors). (bottom) Horizontal convergence (shaded), vertical vorticity (contoured), and ground-relative horizontal wind (vectors), at 0028 UTC and z = 0.25 km AGL in the Argonia case produced using (left) dual-Doppler analysis and (right) EnKF analysis.

vertical vorticity at low levels necessary to initially form intense or long-lived tornadoes (Markowski et al. 2003), the generation of new surges of relatively cold outflow air after tornadogenesis may have assisted with tornado maintenance by baroclinically generating and then tilting horizontal vorticity in the secondary outflow. We speculate that strong vertical motions arising from the interaction of the tornado with the ground (or other dynamic-perturbation pressure gradient forces associated with mesocyclone-scale processes occurring after tornadogenesis) could be sufficient to lift much colder secondary outflow parcels.

Though this work has compared certain attributes of four supercell storms, a more complete understanding of tornado maintenance cannot be attained until a larger sample of cases is examined. Future studies should examine high-resolution kinematic and thermodynamic data collected in many other storms, such as those collected in the Second Verification of the Origins of Rotation in Tornadoes Experiment (VORTEX2) field project, in order to test the hypotheses of tornado maintenance presented in this study. Additionally, future work should attempt to diagnose the cause of multiple rear-flank downdraft surges in supercell

storms, which could not be diagnosed in some of our cases owing to the limited amount of radar data available. A knowledge of these topics will likely increase the skill of forecasts and nowcasts of tornado longevity.

Acknowledgments. This project was funded by NSF Grants ATM-0437512, ATM-0437505, and ATM-0437898. The data assimilation experiments were conducted on NCAR CISL supercomputing facilities using the NCAR Data Assimilation Research Testbed and WRF-ARW software packages. We thank the writers and support staff of these facilities, particularly Nancy Collins, Jeff Anderson, and Chris Snyder. Curtis Alexander, Karen Kosiba, Mario Majcen, Nettie Arnott, and Paul Robinson provided useful analysis scripts and data support that made this work possible. We would also like to thank the writers of the SOLOII and Vis5d routines. We also thank Hans Verlinde, Diane Henderson, and three anonymous reviewers for suggestions on a previous version of this manuscript, and the following individuals for advice and analysis opinions during this research: Glen Romine, Altug Aksoy, Bruce Lee, Cathy Finley, Lou Wicker, Dan Dawson, Jeff Frame, Kent Knopfmeier, and Brian Monahan. Finally, we thank the ROTATE crew for collecting the data analyzed in this article.

APPENDIX

Comparison of Dual-Doppler and EnKF Analyses

Figure A1 compares certain kinematic fields retrieved by dual-Doppler wind synthesis at 0028 UTC and $z = 0.25$ km in the Argonia storm to the same fields produced in the EnKF analysis. To facilitate a more accurate comparison of spatial scales resolved in the data assimilation experiments, the dual-Doppler synthesis in Fig. A1 is produced using DOW velocities that are objectively analyzed using a Cressman weighting with a cutoff radius of 1.0 km (like that used to objectively analyze the assimilated data) and a Cartesian grid spacing of 500 m (same as the model grid spacing). Therefore, the dual-Doppler analysis is coarser than the other dual-Doppler analyses used throughout the study. The analysis shown represents one of the largest volumes of dual-Doppler data available in this case and corresponds to a time when tornadogenesis is imminent.

Despite some subtle differences between the magnitudes of vertical motion in this particular example, there is strong qualitative agreement between the dual-Doppler and EnKF u, v, and w fields; both contain well-defined bands of ascent along the gust fronts and downdraft on the rear flank west and south of the vorticity maximum with strong northwesterly outflow winds. Both methods retrieve a similar peak magnitude of vertical vorticity, although the EnKF analysis produces a more elongated vorticity maximum. The pattern of the horizontal convergence fields also is qualitatively similar, but magnitudes of dual-Doppler convergence–divergence are a bit smaller than EnKF values. These differences appear to result in a more coherent band of low-level convergence along the secondary gust front (5–7 km southwest of the vorticity maximum), which is developing at this time. It is not clear which of these two wind retrieval methods produces a more accurate solution because both contain errors in their calculations. For example, the missing DOW observations near the surface affect the magnitude of the w field produced in the dual-Doppler solution, and an oversimplified representation of PBL and surface processes because of a lack of their parameterization introduces uncertainty in the near-surface wind analyses. It is possible that differences in these two solutions may be within the range of expected variability due to the possible sources of error that are inherent in each method. The qualitative similarities between the EnKF kinematic fields and the dual-Doppler syntheses of similar resolution suggest that the data assimilation results may capture storm-scale processes with sufficient accuracy for the analysis of tornado maintenance.

REFERENCES

Adlerman, E. J., 2003: Numerical simulations of cyclic storm behavior: Mesocyclogenesis and tornado genesis. Ph.D. dissertation, University of Oklahoma, 217 pp. [Available from School of Meteorology, University of Oklahoma, 100 East Boyd, Suite 1310, Norman, OK 73019.]

Aksoy, A., D. C. Dowell, and C. Snyder, 2009: A multi-case comparative assessment of the ensemble Kalman filter for assimilation of radar observations. Part I: Storm-scale analyses. *Mon. Wea. Rev.,* **137,** 1805–1824.

Alexander, C., and J. Wurman, 2008: Updated mobile radar climatology of supercell tornado structures and dynamics. Preprints, *24th Conf. on Severe Local Storms,* Savannah, GA, Amer. Meteor. Soc., 19.4. [Available online at http://ams.confex.com/ams/pdfpapers/141821.pdf.]

Anderson, J., 2001: An ensemble adjustment Kalman filter for data assimilation. *Mon. Wea. Rev.,* **129,** 2884–2903.

——, T. Hoar, K. Raeder, H. Liu, N. Collins, R. Torn, and A. Avellano, 2009: The Data Assimilation Research Testbed: A community facility. *Bull. Amer. Meteor. Soc.,* **90,** 1283–1296.

Barnes, S. L., 1964: A technique for maximizing details in numerical weather map analysis. *J. Appl. Meteor.,* **3,** 396–409.

Brandes, E. A., 1978: Mesocyclone evolution and tornado genesis: Some observations. *Mon. Wea. Rev.,* **106,** 995–1011.

——, 1984: Vertical vorticity generation and mesoscyclone sustenance in tornadic thunderstorms: The observational evidence. *Mon. Wea. Rev.,* **112,** 2253–2269.

Davies-Jones, R., 2006: Tornadogenesis in supercell storms—What we know and what we don't know. Preprints, *Symp. on the*

Challenges of Severe Convective Storms, Atlanta, GA, Amer. Meteor. Soc., P2.2. [Available online at http://ams.confex.com/ams/Annual2006/techprogram/paper_104563.htm.]

——, and H. E. Brooks, 1993: Mesocyclogenesis from a theoretical perspective. *The Tornado: Its Structure, Dynamics, Prediction, and Hazards, Meteor. Monogr.,* No. 79, Amer. Meteor. Soc., 105–114.

Dowell, D. C., and H. B. Bluestein, 1997: The Arcadia, Oklahoma, storm of 17 May 1981: Analysis of a supercell during tornadogenesis. *Mon. Wea. Rev.,* **125,** 2562–2582.

——, and ——, 2002: The 8 June 1995 McLean, Texas, storm. Part II: Cyclic tornado formation, maintenance, and dissipation. *Mon. Wea. Rev.,* **130,** 2649–2670.

——, and A. Shapiro, 2003: Stability of an iterative dual-Doppler wind synthesis in Cartesian coordinates. *J. Atmos. Oceanic Technol.,* **20,** 1552–1559.

——, and L. J. Wicker, 2009: Additive noise for storm-scale ensemble data assimlation. *J. Atmos. Oceanic Technol.,* **26,** 911–927.

——, Y. Richardson, and J. Wurman, 2002: Observations of the formation of low-level rotation: The 5 June 2001 Sumner County, Kansas, storm. Preprints, *21st Conf. on Severe Local Storms,* San Antonio, TX, Amer. Meteor. Soc., 12.3. [Available online at http://ams.confex.com/ams/pdfpapers/47335.pdf.]

——, F. Zhang, L. J. Wicker, C. Snyder, and N. A. Crook, 2004: Wind and temperature retrievals in the 17 May 1981 Arcadia, Oklahoma, supercell: Ensemble Kalman filter experiments. *Mon. Wea. Rev.,* **132,** 1982–2005.

——, C. R. Alexander, J. M. Wurman, and L. J. Wicker, 2005: Centrifuging of hydrometeors and debris in tornadoes: Radar-reflectivity patterns and wind-measurement errors. *Mon. Wea. Rev.,* **133,** 1501–1524.

Emanuel, K. A., 1994: *Atmospheric Convection*. Oxford University Press, 592 pp.

Finley, C. A., and B. D. Lee, 2008: Mobile mesonet observations of an intense RFD and multiple RFD gust fronts in the May 23 Quniter, Kansas, tornadic supercell during TWISTEX 2008. Preprints, *24th Conf. on Severe Local Storms,* Savannah, GA, Amer. Meteor. Soc., P3.18. [Available online at http://ams.confex.com/ams/pdfpapers/142133.pdf.]

——, ——, M. Grzych, C. D. Karstens, and T. M. Samaras, 2010: Mobile mesonet observations of the rear-flank downdraft evolution associated with a violent tornado near Bowdle, SD on 22 May 2010. Preprints, *25th Conf. on Severe Local Storms,* Denver, CO, Amer. Meteor. Soc., 8A.2. [Available online at http://ams.confex.com/ams/pdfpapers/176132.pdf.]

Gaspari, G., and S. E. Cohn, 1999: Construction of correlation functions in two and three dimensions. *Quart. J. Roy. Meteor. Soc.,* **125,** 723–757.

Gilmore, M. S., J. M. Straka, and E. N. Rasmussen, 2004: Precipitation and evolution sensitivity in simulated deep convective storms: comparisons between liquid-only and simple ice and liquid phase microphysics. *Mon. Wea. Rev.,* **132,** 1897–1916.

Grasso, L. D., and W. R. Cotton, 1995: Numerical simulation of a tornado vortex. *J. Atmos. Sci.,* **52,** 1192–1203.

Grzych, M. L., B. D. Lee, and C. A. Finley, 2007: Thermodynamic analysis of supercell rear-flank downdrafts from Project ANSWERS. *Mon. Wea. Rev.,* **135,** 240–246.

Hamill, T. M., J. S. Whitaker, and C. Snyder, 2001: Distance-dependent filtering of background error covariance estimates in an ensemble Kalman filter. *Mon. Wea. Rev.,* **129,** 2776–2790.

Hirth, B. D., J. L. Schroeder, and C. C. Weiss, 2008: Surface analysis of the rear-flank downdraft outflow in two tornadic supercells. *Mon. Wea. Rev.,* **136,** 2344–2363.

Johnson, B. C., 1983: The heat burst of 29 May 1976. *Mon. Wea. Rev.,* **111,** 1776–1792.

Klemp, J. B., and R. Rotunno, 1983: A study of the tornadic region within a supercell thunderstorm. *J. Atmos. Sci.,* **40,** 359–377.

Koch, S. E., M. DesJardins, and P. J. Kocin, 1983: An interactive Barnes objective map analysis scheme for use with satellite and conventional data. *J. Climate Appl. Meteor.,* **22,** 1487–1503.

Lee, B. D., C. A. Finley, and T. M. Samaras, 2008: Thermodynamic and kinematic analysis near and within the Tipton, KS tornado on May 29 during TWISTEX 2008. Preprints, *24th Conf. on Severe Local Storms,* Savannah, GA, Amer. Meteor. Soc., P3.13. [Available online at http://ams.confex.com/ams/pdfpapers/142078.pdf.]

Lemon, L. R., and C. A. Doswell, 1979: Severe thunderstorm evolution and mesocyclone structure as related to tornadogenesis. *Mon. Wea. Rev.,* **107,** 1184–1197.

Lin, Y., R. D. Farley, and H. D. Orville, 1983: Bulk parameterization of the snow field in a cloud model. *J. Climate Appl. Meteor.,* **22,** 1065–1092.

Majcen, M., P. Markowski, Y. Richardson, D. Dowell, and J. Wurman, 2008: Multipass objective analyses of Doppler radar data. *J. Atmos. Oceanic Technol.,* **25,** 1845–1858.

Markowski, P. M., 2002: Mobile mesonet observations on 3 May 1999. *Wea. Forecasting,* **17,** 430–444.

——, J. M. Straka, and E. N. Rasmussen, 2002: Direct surface thermodynamic observations within the rear-flank downdrafts of nontornadic and tornadic supercells. *Mon. Wea. Rev.,* **130,** 1692–1721.

——, ——, and ——, 2003: Tornadogenesis resulting from the transport of circulation by a downdraft: Idealized numerical simulations. *J. Atmos. Sci.,* **60,** 795–823.

——, M. Majcen, Y. Richardson, J. Marquis, and J. Wurman, 2011: Characteristics of the wind field in a trip of nontornadic low-level mesocyclones observed by the Doppler on Wheels radars. *Electron. J. Severe Storms Meteor.,* **5** (7), 1–24.

Marquis, J. N., Y. P. Richardson, J. M. Wurman, and P. M. Markowski, 2008: Single- and dual-Doppler analysis of a tornadic vortex and surrounding storm scale flow in the Crowell, TX, supercell of 30 April 2000. *Mon. Wea. Rev.,* **136,** 5017–5043.

Pauley, P. M., and X. Wu, 1990: The theoretical, discrete, and actual response of the Barnes objective analysis scheme for one- and two-dimensional fields. *Mon. Wea. Rev.,* **118,** 1145–1163.

Rasmussen, E. N., and J. M. Straka, 2007: Evolution of low-level angular momentum in the 2 June 1995 Dimmitt, Texas, tornado cyclone. *J. Atmos. Sci.,* **64,** 1365–1378.

Richardson, Y., D. Dowell, and J. Wurman, 2001: High resolution dual-Doppler analyses of two thunderstorms during the pre-tornadogenesis and mature tornado stages. Preprints, *30th Int. Conf. on Radar Meterology,* Munich, Germany, Amer. Meteor. Soc., 295–297.

Skamarock, W. C., J. B. Klemp, J. Dudhia, D. O. Gill, D. M. Barker, W. Wang, and J. G. Posers, 2005: A description of the advanced research WRF version 2. NCAR Tech. Note TN-468+STR, 88 pp.

Snyder, C., and F. Zhang, 2003: Assimilation of simulated Doppler radar observations with an ensemble Kalman filter. *Mon. Wea. Rev.,* **131,** 1663–1677.

Stonitsch, J. R., and P. M. Markowski, 2007: Unusually long duration, multiple-Doppler radar observation of a front in a convective boundary layer. *Mon. Wea. Rev.,* **135,** 93–117.

Straka, J. M., E. N. Rasmussen, R. P. Davies-Jones, and P. M. Markowski, 2007: An observational and idealized numerical examination of low-level counter-rotating vortices toward the rear flank of supercells. *Electron. J. Severe Storms Meteor.,* **2** (8), 1–22.

Sun, J., and N. A. Crook, 2001: Real-time low-level wind and temperature analysis using single WSR-88D data. *Wea. Forecasting,* **16,** 117–132.

Trapp, R. J., and B. H. Fiedler, 1995: Tornado-like vortexgenesis in a simplified numerical model. *J. Atmos. Sci.,* **52,** 3757–3778.

——, and R. Davies-Jones, 1997: Tornadogenesis with and without a dynamic pipe effect. *J. Atmos. Sci.,* **54,** 113–133.

——, and C. A. Doswell, 2000: Radar data objective analysis. *J. Atmos. Oceanic Technol.,* **17,** 105–120.

Wakimoto, R. M., and B. E. Martner, 1992: Observations of a Colorado tornado. Part II: Combined photgrammetric and Doppler radar analysis. *Mon. Wea. Rev.,* **120,** 522–543.

——, and C. Liu, 1998: The Garden City, Kansas, storm during VORTEX 95. Part II: The wall cloud and tornado. *Mon. Wea. Rev.,* **126,** 393–408.

Wicker, L. J., and R. B. Wilhelmson, 1995: Simulation and analysis of tornado development and decay within a three-dimensional supercell thunderstorm. *J. Atmos. Sci.,* **52,** 2675–2703.

Wurman, J., J. M. Straka, E. N. Rasmussen, M. Randall, and A. Zahrai, 1997: Design and deployment of a portable, pencil-beam, pulsed, 3-cm Doppler radar. *J. Atmos. Oceanic Technol.,* **14,** 1502–1512.

——, Y. Richardson, C. Alexander, S. Weygandt, and P. F. Zhang, 2007a: Dual-Doppler and single-Doppler analysis of a tornadic storm undergoing mergers and repeated tornado-genesis. *Mon. Wea. Rev.,* **135,** 736–758.

——, ——, ——, ——, and ——, 2007b: Dual-Doppler analysis of winds and vorticity budget terms near a tornado. *Mon. Wea. Rev.,* **135,** 2392–2405.

——, K. Kosiba, P. Markowski, Y. Richardson, D. Dowell, and P. Robinson, 2010: Finescale single- and dual-Doppler analysis of tornado intensification, maintenance, and dissipation in the Orlenas, Nebraska, supercell. *Mon. Wea. Rev.,* **138,** 4439–4455.